Distributed Control and Information Exchange for Improved Flight Autonomy of Hybrid Powertrain Drones

by

Miroslav Kosanic

B.S., University of Belgrade, 2019
M.Sc., University of Belgrade, 2020

Submitted to the Department of Electrical Engineering and Computer Science
in partial fulfillment of the requirements for the degree of

MASTER OF SCIENCE

at the

MASSACHUSETTS INSTITUTE OF TECHNOLOGY

May 2024

Authored by:	Miroslav Kosanic Department of Electrical Engineering and Computer Science May 17, 2024
Certified by:	Marija Ilic Adjunct Professor of Electrical Engineering and Computer Science Thesis Supervisor
Accepted by:	Leslie A. Kolodziejski Professor of Electrical Engineering and Computer Science Chair, Department Committee on Graduate Students

Distributed Control and Information Exchange for Improved Flight Autonomy of Hybrid Powertrain Drones

by

Miroslav Kosanic

Submitted to the Department of Electrical Engineering and Computer Science
on May 17, 2024 in partial fulfillment of the requirements for the degree of

MASTER OF SCIENCE

ABSTRACT

This work addresses integrating mechanical dynamics and powertrain energy conversion dynamics in Unmanned Aerial Vehicles (UAVs), focusing on hexacopters with hybrid powertrains. The goal is to maximize fuel savings and achieve that through powertrain regulation. One of factors that influence optimal internal combustion engine (ICE) operation is the passively managed battery, which should have the role of a fast supplementary power source. When the powertrain faces disturbances, ICE efficiency may decrease. The question is whether coordinated information exchange through distributed or decentralized control of the battery can outperform centralized powertrain control, which treats the battery as a disturbance in a component-isolated approach.

The core contributions of this thesis include developing a novel modeling approach that integrates energy conversion dynamics with the mechanical dynamics of the drone. A second contribution of the thesis estimates parameters of nonlinear dynamics, using flight-mission data, and shows theoretical conditions for which the system exhibits time-scale separation. Using an average-parameter model, a composite Linear Quadratic Regulator (LQR) policy with predictive control was implemented and simulated during the cruise phase of flight phase, achieving 4.5% fuel savings by recognizing battery disturbances. This result from the centralized approach is compared to the thesis's third contribution, distributed and decentralized control of the battery, where the two differ as decentralized control is achieved through the local information exchange, while distributed components can obtain needed information from components that they are not directly connected.

Both approaches enable the increase of supplement power from the battery, reducing the demand impact on the generator and ICE and saving fuel. The distributed control is helping aggressively without proper coordination, ending up as non-cooperative control, as it doesn't have information on what is the power that the generator needs. Decentralized approach receives the information of supplement power, and as coordination is embedded in this information coming from the generator, and achieves cooperative control. For the fully charged battery during the cruise phase of the flight, distributed saved approximately 34.56% of the initial fuel, while decentralized control saved 50.05% of the initial fuel in the reservoir.

Thesis supervisor: Marija Ilic
Title: Adjunct Professor of Electrical Engineering and Computer Science

Acknowledgments

The Lord is my shepherd; I shall not want.
He makes me lie down in green pastures.
He leads me beside still waters.
He restores my soul.
He leads me in paths of righteousness for His name's sake.

I want to extend my deepest gratitude to my research advisor, Professor Marija Ilic. Without your guidance, wisdom, and unwavering support, this work would not have been possible. You have inspired me, encouraging me to strive for excellence and pushing me beyond the boundaries of my knowledge and capabilities.

To my parents, Ivan and Vesna, thank you for your unconditional love, sacrifices, and encouragement. You have always been my rock, providing me with the foundation to pursue my dreams. To my brother Vladimir, your constant support and belief in me have been invaluable throughout this journey.

To my beloved girlfriend, Katey, words cannot express how grateful I am for your love, patience, and encouragement. You have been my anchor, my confidant, and my greatest source of strength. Your unwavering support and belief in me have been the driving force behind this achievement.

Even though I walk through the valley of the shadow of death, I will fear no evil,
For You are with me;
Your rod and Your staff, they comfort me.

I would also like to express my gratitude to Dr. Rupamathi Jaddivada for her insightful discussions, guidance, and encouragement. Your work and research contributions have significantly inspired this work.

This work was supported by the MIT Advanced Concepts Committee (ACC) Lincoln Lab Project entitled "Exergy Control for Supplying Mission-Critical Loads." I gratefully acknowledge the contribution of the measurements taken by the Lincoln Lab team lead by Aaron Plotnik, Will Bartlett, and the EESG student Aaron Jones.

You prepare a table before me in the presence of my enemies;
You anoint my head with oil;
My cup runs over.
Surely goodness and mercy shall follow me all the days of my life,
And I will dwell in the house of the Lord forever.

This acknowledgment can't fit all the people who helped me on this journey, so thank you all for your unwavering support, encouragement, and love. This achievement would not have been possible without you.

Contents

Title page **1**

Abstract **3**

List of Figures **9**

List of Tables **11**

Introduction **13**
1.1 State-of-the-Art Methods . . . 14
1.1.1 Hybrid Terrestrial Vehicles . . . 14
1.1.2 Battery Powered Drones . . . 15
1.1.3 Hybrid Powered Drones . . . 16
1.2 Thesis Outline . . . 17

Problem Formulation **18**
2.1 Hybrid drones Architecture . . . 18
2.2 Aerodynamic Modeling . . . 20
2.3 Drone Dynamics Modeling . . . 22
2.3.1 Reference Frames . . . 23
2.3.2 Translational Dynamics . . . 24
2.3.3 Rotational Dynamics . . . 24
2.3.4 Component Model of Drone Dynamics . . . 25
2.4 ICE and Fuel Flow Model . . . 26
2.4.1 Chemical Power and Efficiency in ICE . . . 26
2.4.2 Fuel Flow Model . . . 27
2.5 Problem Statement . . . 29
2.5.1 Research Objectives . . . 32

Data-Informed Parameter Estimation **34**
3.1 Dynamic Model Parameter Estimation . . . 34
3.2 Data-Informed Parameter Upper Bounds Estimation . . . 35
3.3 Kalman Filter Joint State-Parameter Estimation . . . 38

Disturbance-Aware Policy for Fuel Efficient Flight Mission **42**
4.1 Singular Perturbation Decomposition of the Lateral-Fuel Flow Model 42
4.2 Near-Optimal Composite Powertrain Regulation 46
4.3 Disturbance Aware Composite Policy 49

Decentralized Information Exchange for Improved Fuel Savings **52**
5.1 Modular Energy Modeling of Interconnected Systems 52
5.1.1 Integrated Physical, Information, and Control Layers in Energy-Efficient Hybrid Powertrain Systems 52
5.2 Decentralized Interactive Flow of Information 55
5.3 Interactive Energy-Based Interconnection Model 59
5.4 Distributed Information Exchange Battery Regulation 61

Numerical Results **65**
6.1 Parameter Estimation 65
6.2 Composite Near-Optimal Regulation 66
6.3 Distributed Battery Control for Powertrain Regulation 69
6.4 Decentralized Battery Control of Powertrain Regulation 71

Conclusion **75**

References **77**

List of Figures

1.1 A comparison of power and energy density of fuel cell, batteries and other energy sources used to power drones [1] . . . 14
2.1 Powertrain system power flow . . . 19
2.2 Reference frames and hexacopter representation . . . 23
2.3 Modeling of hybrid powertrain through power flow and Tellegens' theorem . . . 26
2.4 Power distribution along the mechanical axis during cruise phase of flight . . . 30
2.5 Current of the generator and battery during the cruise phase of flight . . . 31
2.6 Voltage of the generator and battery during the cruise phase of flight . . . 32
4.1 Consecutive Rate of Change of States . . . 44
4.2 Comparison of Dynamics Speed Based on Rate of Change Variability . . . 45
5.1 The interactive stand-alone model of a closed-loop component i . . . 57
5.2 Two different paradigms of information exchange . . . 61
6.1 Fast subsystem states estimates . . . 66
6.2 Fuel state estimate and fast subsystem estimated parameters . . . 67
6.3 Slow subsystem estimated parameters . . . 68
6.4 Trajectory of the drone in xy-plane under unknown lateral policy control during the cruise phase of the flight mission . . . 69
6.5 Reservoir fuel during the cruise phase of the flight mission . . . 69
6.6 Leftover fuel in the reservoir at the end of the cruise phase comparison a) battery blind policy b) battery aware policy . . . 70
6.7 Ratio of battery participation β for different initial state-of-charge of battery during the cruise part of the flight with distributed control . . . 70
6.8 Shift of battery and generator current due to distributed control for different initial state-of-charge of battery during the cruise part of the flight . . . 71
6.9 Distributed control fuel in the reservoir change during the cruise phase of the flight . . . 72
6.10 Ratio of battery participation β for different initial state-of-charge of battery during the cruise part of the flight . . . 73
6.11 Shift of battery and generator current due to decentralized control for different initial state-of-charge of battery during the cruise part of the flight . . . 74
6.12 Decentralized control fuel in the reservoir change during the cruise phase of the flight . . . 74

List of Tables

6.1 Fast Subsystem Parameters 66
6.2 Slow Subsystem Parameters 67

Introduction

The primary challenge in the broader application of multirotor unmanned aerial vehicles (UAVs), is their limited range and endurance. This issue is prevalent in the multi-rotors compared to ground vehicles or fixed-wing aircraft, primarily due to the specifics of energy demand. Multi-rotors consume significantly more energy to maintain flight, reducing their operational duration and range. This limitation becomes a focal point in applications requiring extended flight times 1.1 and distances, making the efficient management of energy through advanced control strategies like the ones investigated in this thesis, practically important. By focusing on connecting modules that operate internally under different physical laws, the hybrid hexacopter drone can be viewed as a multi-domain energy conversion system. This work has a goal of improving fuel savings, but at the same time guaranteeing stability, and uninterrupted set-point tracking, thus addressing a key barrier in the deployment of multirotor UAVs in various scenarios.

There is a growing need for innovative approaches that can enhance UAV flight autonomy. Hybrid drones demand more sophisticated control and planning mechanisms to enhance operational efficiency and extend flight duration. The motivation for this research stems from a mix of different factors and objectives

1. **Technological Advancements:** Complexities introduced in hybrid drone energy management operations add new challenges. Addressing these challenges requires rethinking existing control and mission planning approaches.

2. **Operational Reliability and Efficiency:** Reliability amidst disturbances consequently necessitates distributed control mechanisms to ensure efficient and extended operations under varying weather conditions.

3. **Extension of Flight Time:** Central to this research is the goal of extending the flight time of hybrid drones through better modeling, prediction, and distributed fuel control methods, drawing parallels to the efficient planning/allocation and hierarchical control of resources at different timescales in renewable energy systems.

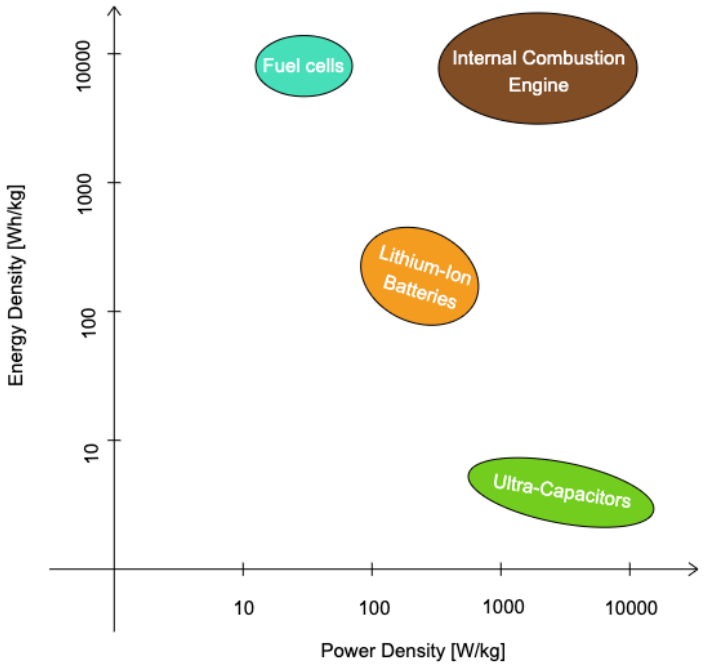

Figure 1.1: A comparison of power and energy density of fuel cell, batteries and other energy sources used to power drones [1]

4. **Environmental Considerations:** The pursuit of environmentally conscious approaches in UAV operations. Incorporating energy-efficient strategies in drone flight missions contributes to broader environmental goals, by reducing the inefficient use of the fuel engine.

1.1 State-of-the-Art Methods

Under the imperative for extended and efficient flight missions the drone transportation sector has evolved from traditional electric drones towards hybrid powertrains. This shift is to be primarily attributed to the still significant disparity in cost-efficiency between battery density and power as seen in Fig. 1.1.

1.1.1 Hybrid Terrestrial Vehicles

The progress in the domain of hybrid terrestrial vehicles showcases a considerable level of maturity. An expansive range of literature, denoted by references delves into the realm of optimal control algorithms specifically tailored for Hybrid Electric Vehicles (HEVs). Parallels can be drawn as similar problems exist within industrial and military drone applications,

but these approaches are not directly transferable to UAVs due to fundamental differences outlined in [2]. These differences necessitate modifications in methods to accommodate for the significant size difference between HEVs and UAVs, different system operating conditions, and disturbances. From an operational standpoint, the requirements of UAVs and HEVs are different thus a need for rapid decision-making in system response that operates on the scale of seconds. For instance, UAVs require the capability to handle sudden surges in power demand, which is distinct from the demands faced by HEVs as their design and region of operation are quite unaffected by disturbances. Additionally, while HEVs can regenerate some battery charge through braking, UAVs lack this feature and must adopt alternative charging methods or prematurely end the flight mission if energy resources are not optimized subject to mission goals.

1.1.2 Battery Powered Drones

There are numerous proposed algorithms for energy-efficient route planning for Unmanned Aerial Vehicles (UAVs) with batteries as the energy source. Despite this, a significant number of these studies overlook a detailed performance evaluation incorporating the battery dynamics. In [3], an energy-aware algorithm is introduced that aims to reduce the total energy consumption of the specific drone configuration. Their algorithm is based on minimizing an objective function that calculates the drone's energy use under various operating conditions through measurements of the absorbed current and the supply voltage and in turn, controls the drone's optimal speed. Similarly, in paper [4] the challenge of finding a minimum-energy path considering the power drawn by the actuators is addressed. This is achieved by optimizing the angular acceleration of a quadrotor's rotors. However, neither study takes into account the electrical energy source. A study [5] delves into the performance of different Lithium Polymer (LiPo) batteries and a comparison is performed for static equations for the battery endurance and experimental data. The research here focuses on four static battery models that consider battery runtime, incorporating aspects like the capacity rate effect and Peukert's law. Their empirical findings highlight a discrepancy when compared to the theoretical predictions of these four models.

In [6] paper, a mathematical model of a hexacopter is derived using Newton-Euler formalism. Using feedback linearization and sliding mode controllers aim is to stabilize the attitude while also tracking the yaw and altitude trajectories of the hexacopter. The result section compares performances, in terms of perturbation rejection, energy consumption, and parameter uncertainties. There was no explicit modeling of the powertrain. A study that includes both fixed-wing and multirotor types, a battery State of Charge (SOC) based altitude

control mechanism is explored in [7]. This approach utilizes a battery model based on the equivalent electrical circuit methodology specifically for Lithium Polymer (LiPo) batteries. Additionally, the study establishes a relationship between the applied thrust of the UAV and its battery SOC. Adjacently, [8] examines route optimization for drone delivery services. The power model proposed in this study, however, primarily accounts for the battery's changing weight along with the payload. Similarly, [9] proposes a model aimed at minimizing the delivery time for a specified number of packages. This model includes considerations of battery performance, but predominantly from the perspective of service duration rather than detailed battery dynamics. In summary, to the best of our knowledge [10] takes into account battery dynamics and establishes a battery-aware model for an accurate energy analysis of the electrically powered drone energy consumption. This line of work's primary concern is energy consumption dependence on distance, and energy consumption dependence on the SOC of the battery while providing accurate SOC estimation.

1.1.3 Hybrid Powered Drones

In the line of work related to hybrid drones [11] is proposing an energy management strategy for hybrid fuel cell/battery-based drones which reduces fuel consumption by 5.1%, extends battery lifespan, and increases autonomy duration. This paper does not explore energy efficiency considering fuel cell/battery dynamics.

In literature, a significant shortcoming of all hybrid models is their lack of modeling the dynamics of internal combustion engines (ICE). Specifically, they operate under the presumption that the engine has enough fuel for the flight mission. This assumption, however, overlooks the complex reality. In practice, an ICE's efficiency varies depending on several factors, including its operational state, such as engine temperature and load conditions. Moreover, the relationship between the demanded power output, ICE's efficiency, and the weather conditions has a significant effect on fuel usage. Consequently, overlooking analysis of the ICE's performance could lead to inaccuracies in predictions about the vehicle's operational duration or range. This is analogous to not modeling battery dynamics [12]. This modeling oversight is particularly crucial when precise knowledge of fuel dynamics and engine efficiency is vital for maximizing drone flight time and distance performance and minimizing environmental impact through fuel savings.

1.2 Thesis Outline

Introduction in Chapter 1 sets the stage by reviewing state-of-the-art methods in hybrid vehicle technologies, with a brief focus on hybrid terrestrial vehicles and battery drones, to finally introduce hybrid drones. The review identifies the research gap in the modeling and control approaches of hybrid powertrains of UAVs. Chapter 2 delves briefly into the architecture and aerodynamic modeling of hybrid drones, highlighting the impact of drag. The chapter extends into comprehensive drone mechanical dynamics modeling, covering reference frames, translational and rotational dynamics, and a component model of drone dynamics. Additionally, it delves into the ICE and fuel flow model, focusing on energy conversion dynamics and power transmission efficiency. The chapter concludes by articulating the problem statement and research objectives. Chapter 3 discusses dynamic model parameter estimation, data-informed parameter upper bounds estimation, and joint state-parameter estimation using the Kalman Filter framework. Focusing on disturbance awareness in terms of fuel reservoir implicit control, Chapter 4 explores the singular perturbation decomposition of the lateral-fuel flow model and presents near-optimal composite powertrain regulation policies. It also discusses the implementation of a disturbance-aware composite policy. The fifth chapter introduces aggregate energy state-space modeling, interactive information exchange, and two control approaches, distributed and decentralized. Part of the chapter discusses the integration and relationship of physical, information exchange, and control layers in hybrid powertrain systems. Chapter 6 presents numerical results, summarizing findings from parameter estimation, and the simulation of composite near-optimal regulation policies. It also showcases the results of distributed and decentralized battery regulation, consolidating the thesis' final contribution into practical recommendations. In the last chapter 7, a summary is given with future research directions.

Problem formulation

This chapter of the thesis first introduces the components of the hybrid powertrain. Such powertrain is most commonly the interconnection of electric motors, electric batteries, and generator, ICE. The battery system provides rapid response and precise control of electric power supplemented to satisfy mechanical system demand and is combined with the robust energy capacity of ICE, to optimize in-flight maneuverability and endurance.

2.1 Hybrid drones Architecture

Hybrid multirotor systems represent a significant leap in aerial technology, combining the agility and precision of electric power with the endurance and robustness of fuel-based systems. This integration has led to the development of more versatile, efficient, and capable multirotor drones, suitable for a wide range of applications, from aerial photography and surveying to cargo delivery and emergency response operations. Among these developments, the integration of hybrid propulsion systems in multi-rotors has emerged as a pivotal innovation, enhancing the performance and efficiency of UAVs.

Hybrid multirotor drones are designed to overcome the limitations inherent in purely electrical or fuel-based systems. This comes with added dynamics and control complexities. The primary goal of the aircraft power supply system in multi-rotors is to deliver ample electrical power for satisfactory in-flight dynamic performance, including efficient maneuvering capabilities, as well as sustained power output to maintain flight for a prescribed duration. Conventionally, purely electric propulsion systems, predominantly utilizing batteries for energy storage and power supply, have been the standard in multirotor aircraft. These systems are characterized by their rapid response time and precise thrust control. However, they are also limited by relatively short flight times and extended recharging periods.

To mitigate these drawbacks, hybrid propulsion systems have been introduced. A hybrid propulsion system in a multirotor vehicle typically consists of at least two synergistic energy sources that collectively contribute to the total power generated within the aircraft's powertrain. This system is designed to ensure efficient energy utilization and optimal performance

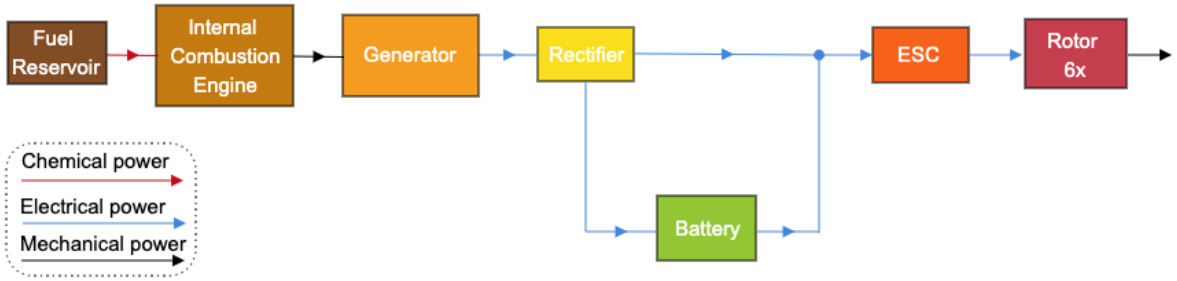

Figure 2.1: Powertrain system power flow

under different external conditions. The power generated by the primary source, like Internal Combustion Engines (ICE), is fed through a power converter and then directed to a common power bus. Similarly, the secondary power source usually the battery, also feeds into this common bus. Additionally, this system facilitates energy transfer between the primary and secondary sources during periods of excess energy.

The design of hybrid multirotor systems allows for different powertrain configurations, including series, parallel, series-parallel, and more complex topologies, each offering distinct advantages and tailored to specific operational requirements. The most common elements in a hybrid system for the multirotor include propellers, electric motors connected through either fixed or variable gear ratio mechanical transmissions, and power converters. These converters can be supplied by a range of sources, such as electrochemical batteries, electricity generators driven by ICE, and in some cases, Photo Voltage (PV) panels and fuel cells. In systems where the power supply is based on a combination of ICE, electrical generator, and battery energy storage, the energy sources are typically the chemical energy of a fuel (like gasoline or methanol) and the electrochemical energy from battery cells. Our system, Harris drone, is one instance of such a system.

The integration of battery energy storage in hybrid systems is particularly advantageous due to its reaction speed and the ability to control output voltage and current through DC-DC power converters. Additional components of such systems include couplings, fuel tanks for the ICE-based generator set, and controllers for the propeller drive electric motors. The main advantage of combining electric propulsion with an ICE-based generator, supplemented by battery energy storage, lies in the ability to achieve rapid response from the propulsion of electric motor drives. This feature allows for significant flexibility in the overall control system of the drone. At the same time, the hybrid system leverages the substantial energy capacity of the ICE, thereby improving flight endurance. The question arises, as to how well the system handles the disturbance and in doing so, how efficiently in terms of fuel

consumption.

2.2 Aerodynamic Modeling

The dynamics of the hexacopter are influenced by several key forces and torques. Thrust force is the force that propels the hexacopter forward and upward, generated by the rotors. It is essential for overcoming the weight of the vehicle and any aerodynamic drag, enabling the hexacopter to hover, climb, and move horizontally. Drag force opposes the motion of the hexacopter through the air, caused by air resistance, and tends to slow down the vehicle. The amount of drag experienced by the hexacopter is influenced by its design, including its shape and surface characteristics. Drag torque is a rotational force arising due to drag on the spinning rotors, affecting the rotational stability and control of the hexacopter, especially when changing direction or speed. Similarly, thrust torque is a rotational force associated with the generation of thrust by the rotors, playing a role in the hexacopter's ability to maneuver and maintain stability during flight.

Thrust Force

The ability of a hexacopter to maintain stability and maneuver is fundamentally linked to its ability to generate sufficient thrust. In the body-fixed frame of the hexacopter, the total thrust force is a cumulative result of the contributions from each of the rotors. This relationship is expressed as follows:

$$T_{\text{thrust}} = \sum_{i=1}^{6} T_i = \sum_{i=1}^{6} k_{\text{thrust}} \omega_i^2 \mathbf{e}_3 \tag{2.1}$$

In Equation (2.1), T_{thrust} represents the total thrust force generated by all rotors Fig. 2.2 ($T_i,\ \forall i \in \{1, \ldots, 6\}$), measured in Newtons [N]. The thrust coefficient, denoted as k_{thrust}, is a key parameter determined by the characteristics of the propeller and motor, and it is measured in Newtons per square radian [N/rad^2]. The term ω_i refers to the angular velocity of the i-th rotor, measured in radians per second (rad/s). At the same time, $\mathbf{e}_3$ is the unit vector along the hexacopter's vertical axis, pointing upwards. The thrust coefficient, k_{thrust}, is important as it defines the relationship between the rotor speed and the generated force. It varies based on several factors, including the propeller's diameter, its pitch angle, and the motor's efficiency. Generally, higher values of k_{thrust} indicate a greater generation of thrust force for a given rotor speed. This relationship is central to understanding how changes in rotor dynamics can directly impact the hexacopter's lift and maneuvering capabilities.

For instance, adjusting the rotor speed can modulate the thrust force, allowing for better control over the hexacopter's vertical and horizontal movements. This control is essential for performing precise aerial maneuvers, maintaining stability in varied atmospheric conditions, and achieving efficient flight dynamics in terms of both energy consumption and aerodynamic performance.

Drag Force

Drag force is the aerodynamic resistance encountered by a hexacopter as it moves through the air, opposing the direction of motion and acting to slow down the drone. This force is critical in determining the hexacopter's performance, as it directly impacts the drone's speed and energy efficiency. As was experimentally explored each axis is affected by the drag force to a certain degree. The drag force is quantified by the equation:

$$F_{\text{drag},i} = \frac{1}{2}\rho v_i^2 C_{D,i} A_i \tag{2.2}$$

where $i \in \{x, y, z\}$, ρ represents the air density [kg/m^3], v is the relative speed of the drone to the wind speed or otherwise called airspeed [m/s] along i-th axis, $C_{D,i}$ is the drag coefficient which depends on the hexacopter's shape and surface properties, and A_i is the reference area along i-th axis [m^2].

The problem of Eq. 2.2 is to find the reference area and the drag coefficient. Depending on the regime determined based on the velocity of the drone, there are two lumped models described in the literature [13], derived from empirical findings that approximate 2.2:

- from $0 - 6m/s$ linear drag where $F_{drag,i} = bv_i$
- from $8 - 12m/s$ quadratic drag where $F_{drag,i} = bv_i^2$

Drag Torque

Drag torque is a rotational force arising from aerodynamic resistance acting on the spinning rotors of the hexacopter. It opposes the rotation of the rotors and plays a significant role in the vehicle's stability and control, particularly during maneuvers involving rapid directional or speed changes. The following equation describes the drag torque:

$$\tau_{\text{drag}} = k_{\text{drag}} \omega_i^2 \tag{2.3}$$

In this equation, k_{drag} is the drag torque coefficient, which is influenced by the rotor design and airfoil characteristics. The term ω_i represents the angular velocity of the i-th rotor

(in rad/s). This torque is crucial in the overall dynamics of the hexacopter, affecting its rotational stability.

Importance of Thrust in Canceling Drag Effects

Drag thrust refers to the part of the total thrust force that is generated to oppose and overcome the drag force, playing a vital role in maintaining the hexacopter's forward motion and stability. This component becomes particularly important in high-speed flights or windy conditions. The relationship between drag thrust and drag force is given by:

$$F_{\text{drag, thrust}} = F_{\text{drag}} \tag{2.4}$$

This equation highlights the direct relationship between drag thrust and drag force, indicating that a significant portion of the thrust generated by the hexacopter is used to counteract the effects of drag.

The presence of drag force and drag torque significantly impacts the dynamics of a hexacopter. Drag force reduces the acceleration and speed, necessitating an increase in thrust to maintain desired velocities. Drag torque can affect the hexacopter's attitude stability, requiring control adjustments to maintain desired orientations. Additionally, increased drag leads to higher energy consumption, as more power is needed to overcome aerodynamic resistance and maintain speed or altitude. Minimizing drag is a complex optimization task that can enhance the hexacopter's performance and efficiency. Strategies for drag reduction include streamlining the hexacopter's body shape and optimizing rotor designs to significantly lower the drag coefficient. Managing velocity by operating at lower relative speeds can effectively reduce the drag force quadratically, leading to improved energy efficiency. Furthermore, flight path optimization, such as avoiding strong headwinds, tailwinds crosswinds, and wind gusts, can effectively lessen the impact of drag on flight dynamics.

2.3 Drone Dynamics Modeling

The hexacopter features six rotors, each positioned at the terminal point of the drone body frame. This design facilitates six degrees of freedom, which consist of three translational and an equal number of rotational motions. Two distinct coordinate systems are utilized to comprehensively characterize the hexarotor's dynamics, as depicted in Figure 2.2. These are the Earth-fixed frame, denoted as E, and the body-fixed frame, with a subscript B.

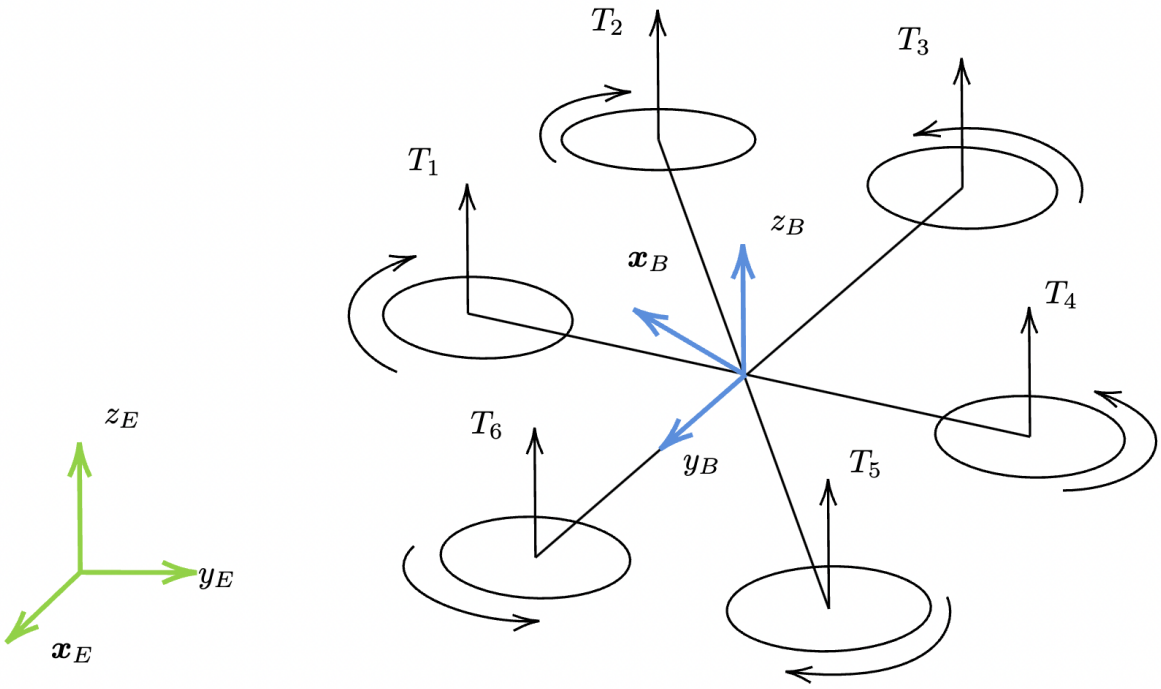

Figure 2.2: Reference frames and hexacopter representation

2.3.1 Reference Frames

Depending on the use, aerial vehicle dynamics define the body-fixed frame and the Earth-fixed frame.

The Earth-fixed reference frame (EFRF), often referred to as the inertial frame or global frame, is a coordinate system that is fixed relative to the Earth. This frame is typically used to describe the position and velocity of the drone, such as its latitude, longitude, and altitude. The axes of the earth frame are usually defined concerning the Earth's surface, with one axis pointing towards true north, another pointing towards east, and the third axis perpendicular to the Earth's surface, pointing upwards.

The body-fixed reference frame (BFRF), is a coordinate system that is fixed relative to the drone itself. Coordinate system moves and rotates with the drone. The axes of the body frame are typically aligned with the drone's principal axes, forward (nose of the drone), right (wingtip direction), and down (perpendicular to the wings, pointing towards the Earth). The body frame will be used to analyze the drone's movements (roll, pitch, yaw), forces, and moments acting directly on it.

For tasks involving navigation and path planning, the EFRF is commonly selected due to its global perspective and stability. In contrast, when addressing attitude control and stabilization, the BFRF is typically the preferred choice, as it directly relates to the drone's

orientation and movements. For more complex operations such as executing advanced maneuvers and navigating around obstacles, a synergistic approach that integrates both the EFRF and BFRF is often necessary. Control algorithms employ a blend of these two reference frames, the Earth-fixed and body-fixed perspectives, to ensure comprehensive and adaptable control of the drone. This integration is essential for optimizing navigation, maintaining stability, and enhancing maneuverability across diverse flight conditions.

For modeling and control purposes, it's often more practical to use the body frame. This is because, in the body frame, the equations of motion are usually simpler and more intuitive to understand and manipulate, especially when dealing with rotational dynamics and forces like thrust, drag, and lift that act directly on the drone.

2.3.2 Translational Dynamics

In the body reference frame, the translational dynamics of the hexacopter are interpreted through the lens of internal forces and movements. This frame is attached to the hexacopter itself, rotating and translating with it. The equation of motion, derived from Newton's second law in this frame, is given by:

$$m\ddot{\mathbf{b}} = \mathbf{F}_{\text{gravity}} + \mathbf{F}_{\text{thrust}} + \mathbf{F}_{\text{drag}} \tag{2.5}$$

Here, m denotes the hexacopter's mass (kg), and $\mathbf{b} = [\mathbf{x}, \mathbf{y}, \mathbf{z}]$ is its body-centric position vector (m). The force $\mathbf{F}_{\text{gravity}}$ represents the gravitational influence in the body frame, while $\mathbf{F}_{\text{thrust}}$ and $\mathbf{F}_{\text{drag}}$ are the thrust and drag forces, respectively, relative to the hexacopter's axes (N).

This body frame-based formulation is crucial for understanding and controlling the hexacopter's flight dynamics. It directly links the hexacopter's propulsion system and aerodynamic characteristics with its translational behavior, facilitating precise maneuvering and stability in aerial operations. By modulating the rotors' output, pilots can navigate efficiently, adapting to the dynamics of flight as experienced from the hexacopter's frame of reference.

2.3.3 Rotational Dynamics

The rotational dynamics of the hexacopter, on the other hand, are dictated by Euler's equation. This equation establishes a relationship between the hexacopter's angular velocity $\boldsymbol{\omega}$ and the torques acting upon it. Expressed mathematically, the rotational dynamics can

be represented as:

$$\mathbf{I}\dot{\boldsymbol{\omega}} + \boldsymbol{\omega} \times (\mathbf{I}\boldsymbol{\omega}) = \boldsymbol{\tau}_{\text{thrust}} + \boldsymbol{\tau}_{\text{drag}} \tag{2.6}$$

Here, $\mathbf{I}$ is the hexacopter's inertia tensor, reflecting its mass distribution and its inherent resistance to changes in rotational motion (kg m^2). The angular velocity vector $\boldsymbol{\omega} = [\dot{\boldsymbol{\phi}}, \dot{\boldsymbol{\theta}}, \dot{\boldsymbol{\psi}}]$ (rad/s) describes the hexacopter's rotational speed and direction. The torques $\boldsymbol{\tau}_{\text{thrust}}$ and $\boldsymbol{\tau}_{\text{drag}}$, represent the total torques generated by the rotors and the aerodynamic drag torque acting on the hexacopter, respectively. These torques are crucial in determining the hexacopter's ability to perform complex maneuvers such as turns and pitch adjustments. By adjusting the differential speeds of the rotors, the pilot can induce controlled rotations around various axes, enhancing the hexacopter's agility and responsiveness.

2.3.4 Component Model of Drone Dynamics

The following equations represent the 6DOF (six degrees of freedom) dynamics of the drone, described in the body reference frame:

$$m\ddot{x} = F_{\text{x}} - F_{\text{drag}_x} \tag{2.7}$$
$$m\ddot{y} = F_{\text{y}} - F_{\text{drag}_y} \tag{2.8}$$
$$m\ddot{z} = F_{\text{z}} - mg - F_{\text{drag}_z} \tag{2.9}$$
$$I_x\ddot{\phi} = \tau_\phi - (\dot{\theta}\dot{\psi}(I_y - I_z)) \tag{2.10}$$
$$I_y\ddot{\theta} = \tau_\theta - (\dot{\phi}\dot{\psi}(I_z - I_x)) \tag{2.11}$$
$$I_z\ddot{\psi} = \tau_\psi - (\dot{\phi}\dot{\theta}(I_x - I_y)) \tag{2.12}$$

In these equations $\ddot{x}$, $\ddot{y}$, $\ddot{z}$ represent the accelerations along the drone's body-fixed axes (x, y, z). F_{x} is the thrust force component along x-axis, while F_{y} and F_{lift} are the components along y-axis and z-axis, respectively. F_{drag_x}, F_{drag_y}, F_{drag_z} are the drag forces experienced along each axis. $\ddot{\phi}$, $\ddot{\theta}$, $\ddot{\psi}$ denote the rotational accelerations around the roll, pitch, and yaw axes of the drone. τ_ϕ, τ_θ, τ_ψ are the torques about these axes. I_x, I_y, I_z are the moments of inertia about the roll, pitch, and yaw axes.

$$F_{\text{x}} = T_{\text{thrust}}(\cos(\theta)\cos(\psi) + \sin(\phi)\sin(\theta)\sin(\psi)) \tag{2.13}$$
$$F_{\text{y}} = T_{\text{thrust}}(\cos(\theta)\sin(\psi) - \sin(\phi)\sin(\theta)\cos(\psi)) \tag{2.14}$$
$$F_{\text{z}} = T_{\text{thrust}}(\cos(\phi)\sin(\theta)) \tag{2.15}$$

Here, T_{thrust} represents the total thrust generated by all rotors. The angles θ (pitch), ϕ (roll), and ψ (yaw) are used to calculate how this total thrust vector is oriented concerning the drone's body frame. These equations assume that the total thrust vector is initially aligned with the drone's vertical axis and that pitch, roll, and yaw movements tilt this vector accordingly. This representation simplifies the model by not considering the individual thrusts and orientations of each rotor, but instead, it focuses on how the overall orientation of the drone (as determined by yaw, roll, and pitch) affects the direction of the total thrust force. This is a common approach in many control systems for drones, as the emphasis is on controlling the overall position and orientation of the drone.

2.4 ICE and Fuel Flow Model

This section delves into the complexities of modeling the Internal Combustion Engine (ICE) for hybrid multirotors. Tellegen's general multi-domain power theorem [14] provides a framework for understanding the interplay between different energy domains within the hybrid system. Under the assumption of minimal losses and instantaneous energy conversion, this theorem tells us that the power flowing from the chemical domain (fuel) must be equivalent to the power in the mechanical domain (engine output) and ultimately, the electrical domain used to power the motors. This principle guides the modeling of the hybrid powertrain, ensuring energy conservation and consistency across its components.

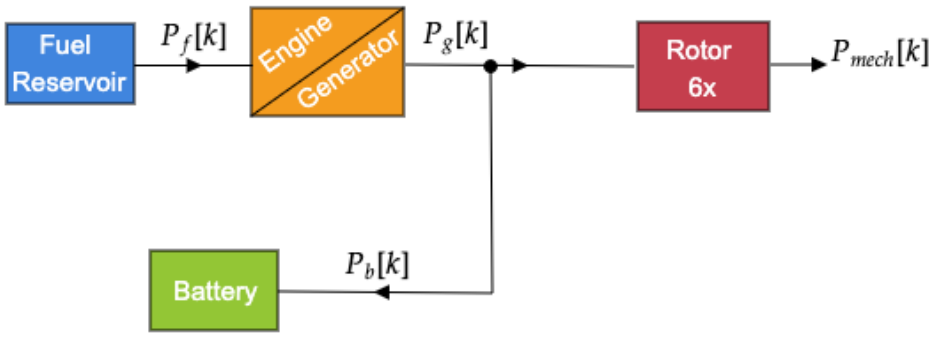

Figure 2.3: Modeling of hybrid powertrain through power flow and Tellegens' theorem

2.4.1 Chemical Power and Efficiency in ICE

The goal of energy conversion is to understand the balance between fuel consumption, mechanical power output, and the inherent inefficiencies of the internal combustion process.

Modeling of Internal Combustion Engine (ICE), particularly for UAV applications, can be done through understanding the power exchanges along the way of the power flow as can be seen in Fig. 2.1. Conversion of the chemical to mechanical power is captured through the relationship as in Eq. 2.16, which links the engine torque T_e measured in $[Nm]$ and the chemical power P_c measured in $[W]$, factoring in the engine's efficiency η. This efficiency, a function of various parameters, plays an important role in determining the engine's performance. The balance equation is

$$wT_e = \eta(\cdot)P_c = \eta(\cdot)\dot{f}H_{LV} \tag{2.16}$$

where w denotes the engine speed rad/s, $\dot{f}$ represents the fuel mass flow rate in the units of $[kg/s]$, and H_{LV} is the lower heating value of the fuel $[J/kg]$. The efficiency $\eta(\cdot)$, not explicitly specified, is influenced by factors such as engine load, fuel type, and environmental conditions. An affine approximation of this efficiency is utilized as

$$T_e = eH_{LV}\dot{f}/w - T_{\text{loss}} \tag{2.17}$$

where e represents the engine's inherent thermodynamic efficiency and T_{loss} accounts for internal engine losses. This establishes a linear relationship with a constant term between the torque and fuel mass per cycle and is particularly effective in highlighting the trend of decreasing efficiency at lower torque levels. The term $eH_{LV}\dot{f}/w$ in Equation (2.17) symbolizes the theoretical torque, assuming complete conversion of chemical energy to mechanical energy. However, the actual torque is reduced by T_{loss}, which quantifies the internal engine losses. These losses include factors such as friction, heat dissipation, and inefficiencies in the fuel combustion process, but also the disturbances from interconnection.

While the affine approximation simplifies the complex relationship between efficiency, torque, and fuel consumption, it is generally accurate for modeling ICE behavior in UAVs, offering a good approximation approach to understanding engine dynamics.

2.4.2 Fuel Flow Model

The connection between fuel flow rate and rotor power, which ultimately leads to thrust is now derived. This derivation is made under the assumptions of the minimal electrical and mechanical losses approach for real power exchange between systems, as outlined in [15], and under the application of Tellegen's theorem to maintain the balance of real power at ports within the context of UAV dynamics. This analysis takes into account the efficiency and losses in various components while ensuring that the sum of power inputs and outputs

in the system remains equal. Given the equation for engine torque

$$T_e = eH_{LV}\dot{f}/w - T_{\text{loss}} \tag{2.18}$$

and assuming negligible T_{loss}, the equation simplifies to:

$$T_e = eH_{LV}\dot{f}/w \tag{2.19}$$

Now, consider the connection between engine torque T_e and the power output of the engine P_e. The power output can be defined as:

$$P_e = T_e \times w = P_{el} \tag{2.20}$$

Substituting Eq. (2.19) into Eq. (2.20) it follows

$$P_{el} = vi = \kappa(\cdot)(P_e + P_b) = (eH_{LV}\dot{f}/w) \times w = eH_{LV}\dot{f} \tag{2.21}$$

where P_b is the battery power, while the whole equation represents the total mechanical power output of the engine based on the fuel flow rate $\dot{f}$ that is converted to electrical power which will be connected to the power provided to the mechanical subsystem.

Under the assumption of minimal electrical losses, the power used by the rotors is almost equal to the mechanical power output of the engine. If P_{mech} represents the power used by the rotors, with each i representing translational axis of the drone, then

$$P_{mech} \approx \sum_i \psi_i F_i v_i = \zeta(\cdot) P_{el} \tag{2.22}$$

Thus, combining Eq. (2.22) and Eq. (2.21), a connection between the fuel flow rate $\dot{f}$, the power generated by the mechanical translational axes and the battery power is established and one can write

$$\sum_i \psi_i F_i v_i - \eta P_b = keH_{LV}\dot{f} \tag{2.23}$$

or

$$\dot{f} = \frac{-\sum_i \psi_i F_i v_i - \eta P_b}{keH_{LV}} = -\alpha F_x v_x - \beta F_y v_y \tag{2.24}$$

The minuses are present as the power is a demand proportional to the needed force that moves the drone along each axis with a certain velocity. This equation represents how the

fuel flow rate $\dot{f}$ is ultimately influenced by the thrust generated by the rotors of a UAV, assuming minimal losses in the powertrain and electrical systems, and using the principles of Tellegen's theorem.

In addition to the relationship described above, fuel flow dynamics can be further extended to account for internal dynamics lag. The lag factor, denoted as $-\frac{1}{T_f} \cdot f$, represents the time delay or internal dynamics associated with fuel flow. When considering this lag, the modified equation connecting the fuel flow rate $\dot{f}$ to the thrust generated by the rotors becomes:

$$\dot{f} = -\alpha(\cdot)F_x v_x - \beta(\cdot)F_y v_y - \gamma(\cdot)P_b - \frac{1}{T_f}f \tag{2.25}$$

Here, $-\frac{1}{T_f} \cdot f$ represents the internal dynamics time constant of the fuel flow, and it affects the rate of change of fuel flow over time. Coefficients $\alpha(\cdot)$, $\beta(\cdot)$, and $\gamma(\cdot)$ have a meaning of the power transmission coefficients (accumulated system inefficiencies) along the power flow of the power train. From now the brackets will be dropped such that $\alpha,\ \beta,\ \gamma$.

2.5 Problem Statement

The objective of this research is to address a challenge in the dynamics modeling of drones, focusing on the connection between drone powertrain and mechanical subsystems under varying operational conditions. The thesis aim is to develop a holistic nonlinear model, that effectively captures powertrain dynamics and the mechanical subsystem dynamics. This model aims to account for the effects of varying aerodynamic disturbances, such as drag, but mainly the effects of downstream load on upstream energy sources and the coordination of energy sources between themselves as the interaction with the interconnected system. This integration should significantly enhance the understanding of UAV performance across a range of flight conditions. As the model is nonlinear, there is a question of linearization that can be circumvented if one projects onto linear state-space, which then asks for interactive aggregate energy-state modeling. This model captures the first and second-order effects of energy conversion, accounting for transients between interconnected components. It is important to highlight under which assumptions, for which components are equations valid, and at which sampling rates. This is important for understanding interconnection stability and the effect of components on each other over time.

Assumptions: The modeling of the powertrain's energy dynamics in the hybrid UAV operates under several key assumptions to streamline the analysis. Firstly, energy conversion within the system is assumed to be instantaneous, meaning that no component, other than

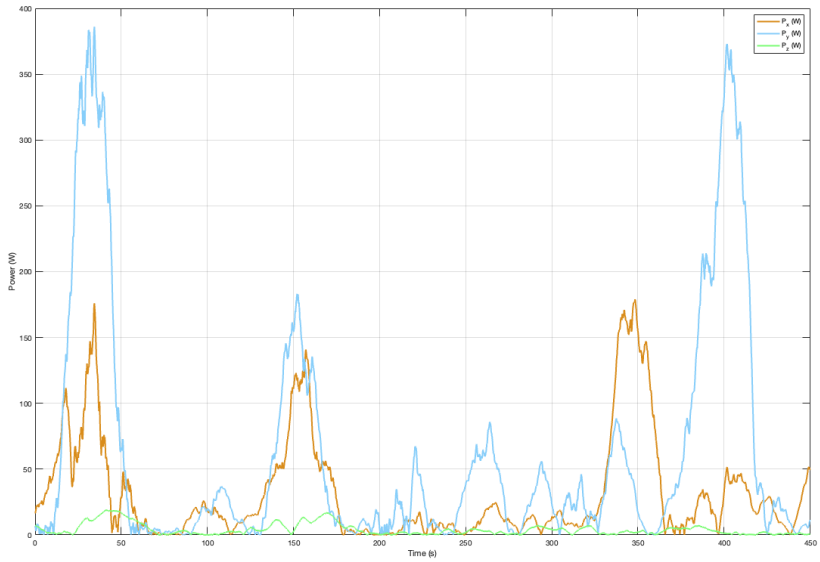

Figure 2.4: Power distribution along the mechanical axis during cruise phase of flight

the fuel reservoir, stores energy. This includes the fuel engine, generator, and mechanical subsystem. The battery is to be assumed to have the initial charge at the beginning of the drone's cruise period at the constant height and is capable of dynamically redistributing current to meet the powertrain's immediate needs. The battery is assumed to be an interface that can provide needed power but the discharge rate and stored energy of the battery capacity have physical limits. Additionally, the mechanical subsystem is designed with negligible inertia, allowing the rotors to change rotation direction quickly, thereby assuming zero stored energy. The slow dynamics of the fuel reservoir imply that its second-order energy stored energy dynamics effects are negligible. Furthermore, the battery is characterized as a fast process relative to the generator and it's acting passively. Due to a sampling time of $\Delta T = 0.1$ seconds, transients within the system are averaged, obscuring the interactiveness of the components during simulations and operational analysis.

Problem: The dynamics of the hybrid powertrain of UAVs, particularly hexacopters, are complex and influenced by multiple interacting factors such as fuel flow dynamics, battery charging/discharging cycles, and downstream load demand. Current drones often fail to integrate these aspects holistically as by their manufacturing design, each component is made to operate robustly in the prescribed ranges leading to the suboptimal performance in varying operational conditions. This thesis explores a gap in the systematic modeling of powertrain dynamics, comparing and challenging the centralized control approach against distributed and decentralized control through information exchange between components. The systems

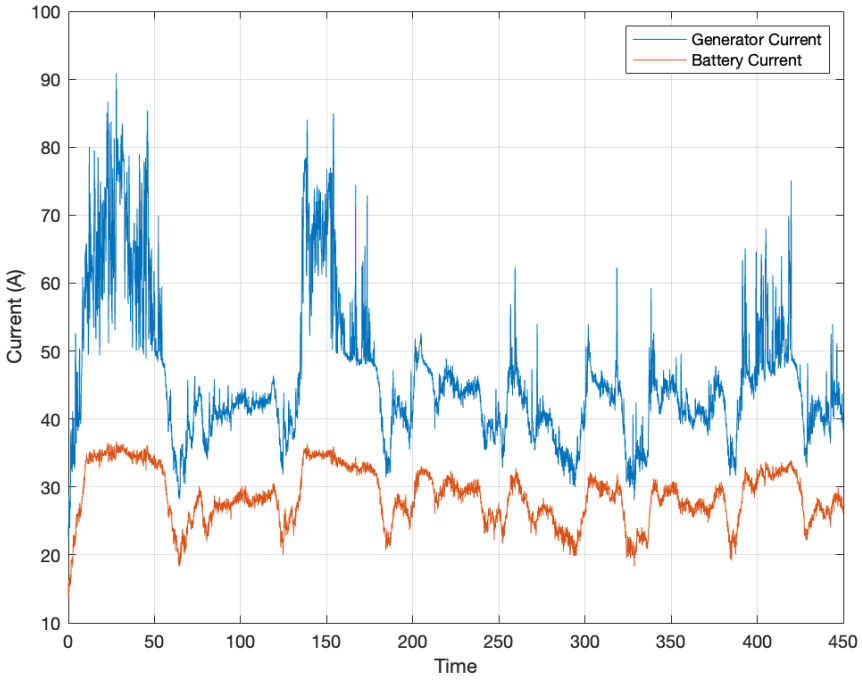

Figure 2.5: Current of the generator and battery during the cruise phase of flight

view of the interconnected powertrain with its integrated control and flight dynamics control is important from the standpoint of optimizing for fuel savings and improved operational stability under diverse flight conditions. The mentioned component design propagates to control through centralized information collection and requires high gain controllers of each component which potentially can destabilize the system. This approach is thus constraining and is challenged by the distributed and decentralized control of components.

Coming from the data, a hypothesis is that suboptimal operation of the generator and then consequently the engine propagates to inefficient use of the fuel. Such premise comes from the hypothesis that lateral dynamics Fig. 2.4 impact the regulation of the powertrain under the passive operation of the battery component. The model that captures both processes is initially formulated in a centralized manner as a state-space model that includes lateral position x and y, lateral speed v_x and v_y, and fuel flow f, with the battery power viewed as a disturbance from the perspective of the powertrain. The model equations are defined as follows:

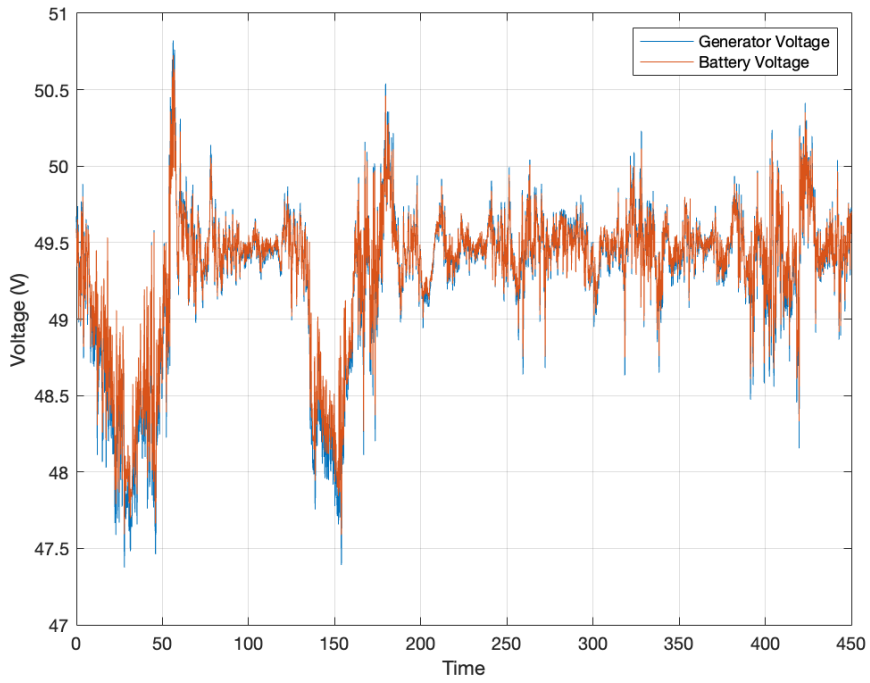

Figure 2.6: Voltage of the generator and battery during the cruise phase of flight

$$\dot{x} = v_x, \qquad x(0) = x_0 \tag{2.26}$$

$$\dot{y} = v_y, \qquad y(0) = y_0 \tag{2.27}$$

$$\dot{v}_x = \frac{1}{m}F_x - \frac{b_x}{m}v_x, \qquad v_x(0) = v_{x,0} \tag{2.28}$$

$$\dot{v}_y = \frac{1}{m}F_y - \frac{b_y}{m}v_y, \qquad v_y(0) = v_{y,0} \tag{2.29}$$

$$\dot{f} = -\alpha F_x v_x - \beta F_y v_y - \gamma P_b - \frac{1}{T_f}f, \qquad f(0) = f_0 \tag{2.30}$$

This modeling will be addressed from another perspective later in Section 5.1 where interactive energy-state space will be introduced, as this modeling framework doesn't require linearization.

2.5.1 Research Objectives

Building on the identified challenges in hybrid UAV dynamics, this thesis aims to:

- Develop a holistic model that captures the dynamics of the powertrain energy conversion with the mechanical subsystem dynamics, enhancing operational efficiency and

thus the saved fuel

- Estimate average model parameters as the system is of the class of the time-varying systems and approximate the upper-bound of the parameters to confirm the existence of time-scale separation

- Implement and simulate the system using the centralized composite control strategy that near-optimally manages energy consumption and responds adaptively to battery disturbances

- Implement and simulate distributed and decentralized control with interactive information flow, and compare achieved fuel savings. The goal is to optimize the current discharge distribution of the battery and reduce the demand on the generator, as currently seen in Fig. 2.5

Data-Informed Parameter Estimation

3.1 Dynamic Model Parameter Estimation

Parameter estimation for ordinary differential equation (ODE) models is a challenging task across various scientific and engineering disciplines [16]. The objective is to determine the parameter values that best fit a model to an observed dataset, typically by minimizing the difference between the model predictions and the data. Among the various approaches, the least squares method is extensively utilized due to its robustness and optimal guarantees.

The least squares approach to parameter estimation in ODE models involves minimizing the sum of the squares of the differences between observed values and those predicted by the model:

$$\min_{\theta} \sum_{k=1}^{n} \left(y_k - f(x_k, u_k; \theta)\right)^2 \tag{3.1}$$

where y_k are the observed data points at times $k\Delta T$, $f(x(t), u(t); \theta)$ represents the continuous model predictions parameterized by θ, system input $u(t)$ at discrete k-th time moment $k\Delta T$ when measurement was sampled, and n is the number of data points sampled during the evolution of the system.

Most parameters in dynamic systems cannot be directly measured and could be estimated through correlations between parameters and errors in state variables. This situation is similar to that of state variables that are not directly observed but can be estimated from the measurements of other state variables that are connected to them. If there is a significant error covariance between the observed variables and a particular parameter, this indicates that the parameter strongly influences the observed variables. In such cases, the parameter can be effectively estimated from these observations. When a parameter can be reliably estimated in this manner, it is referred to as being identifiable.

General description of the model system, given by a set of first-order differential equations

with parameters

$$\dot{x}_1(t) = f_1(t, x_1(t), x_2(t), \ldots, x_n(t), u(t); \theta_1, \ldots, \theta_m) \tag{3.2}$$
$$\dot{x}_2(t) = f_2(t, x_1(t), x_2(t), \ldots, x_n(t), u(t); \theta_1, \ldots, \theta_m) \tag{3.3}$$
$$\vdots$$
$$\dot{x}_n(t) = f_n(t, x_1(t), x_2(t), \ldots, x_n(t)u(t); \theta_1, \ldots, \theta_m) \tag{3.4}$$

In vector notation, the system can be written as

$$\dot{x}(t) = f(t, x(t), u(t); \theta) \tag{3.5}$$

The parameter vector $\theta \in R^m$ contains all parameters of both the system and the measurement function. The observed state $x(t) \in R^n$ cannot be measured directly; instead, what is observed is the quantity $y(t)$, which is related to $x(t)$ through a smooth measurement function plus some independent random errors $\eta(t)$. Measurements are performed at discrete times, typically at uniform intervals. This setup can be described more succinctly by introducing a measurement equation:

$$y_t = G(x_t, u(t), \theta) + \eta_t \tag{3.6}$$

resulting in a multivariate time series $y_{t_i} (i = 1, \ldots, N)$. The challenge then becomes to estimate both the states $x(t)$ at any desired time and the parameters θ, framing this as a dynamical system identification problem [17].

The problem can be formulated as follows, where given a n-dimensional time series y_k (for $k = 1, 2, \ldots, N$) and the model functions described in Eqs. (3.5) and (3.6), the task is to estimate the states x_k for any given time $k\Delta T$ and the parameters θ. However, before delving deeper into the identification methods, it is crucial to consider the practical limitations imposed by the availability of data. Specifically, understanding the bounds of our parameters becomes essential when one is faced with limited data and domain knowledge of the system, a common scenario in many cyber-physical systems.

3.2 Data-Informed Parameter Upper Bounds Estimation

An important aspect of most cyber-physical systems is that the domain of the system is bounded because of physical constraints. This means that both the states and parameters have to be within certain limits defined by the physical capabilities and safety requirements

of the system, applicable to both offline and online analysis First, a known results are introduced, by stating the Extremum Value Theorem and known extension of the Picard-Lindelof theorem that combined guarantees the solution of a perturbed system is unique and exists.

Theorem 1: Assume that K is a compact subset of $\mathbb{R}^n$, and that $f : K \to \mathbb{R}$ is continuous. Then, the set $\{f(x) : x \in K\}$ is compact, and there exist x^+ and x^- in K such that

$$f(x^+) = \sup\{f(x) : x \in K\}$$
$$f(x^-) = \inf\{f(x) : x \in K\}$$

When there exists x^+ as in the equation above, one can say that f attains its supremum, and when there exists x^-, one can say that f attains its infimum [18].

This theorem guarantees that a continuous function on a compact domain is bounded and attains its bounds within that interval.

Theorem 2 Let $G = D \times [t_0, T] \times (0, \varepsilon_0]$, where $D \subset R^n$ is an compact subset of Euclidian space. Consider the differential equation

$$\dot{x} = f(x, t, \varepsilon) \tag{3.7}$$

One is interested in solutions x of this equation with initial value $x(t_0) = x_0$. Let $D = \{x \in \mathbb{R}^n \mid \|x - a\| < d\}$, inducing G and $f : G \to \mathbb{R}^n$. If one assume that f is continuously differentiable on G then the initial value problem has a unique solution x which exists for $t \leq t_0 + \inf(T, d/M)$ where $M = \sup_G \|f\|_{\sup}$.

Condition that the function is differentiable establishes the existence of derivatives. Continuity implies the finite value of the derivative according to the Extreme Value Theorem, as a continuous function on a compact domain must have be bounded. In cyber-physical system variables of interest can't "jump" instantaneously due to the laws of physics. This provides continuity, but for compactness to be satisfied, a system has to have predefined operational constraints which guide the experiment. If these two conditions are satisfied, then one can extend previous theorems naturally to define the notion of upper-bound of system parameters.

The general form of the multi-scale quasi-linear system is given by:

$$\frac{dx_f}{dt} = g(x_f, x_s, u, t) \tag{3.8}$$
$$\frac{dx_s}{dt} = \epsilon f(x_f, x_s, u, t) \tag{3.9}$$

where $x_f \in K_{x_f}$, $x_s \in K_{x_s}$, and $u \in K_u$, with K_{x_f}, K_{x_s}, and K_u being compact subsets of their respective Euclidean spaces. The functions are defined as $g : K_{x_f} \times K_{x_s} \times K_u \times \mathbb{R} \to K_{x_s}$ and $f : K_{x_f} \times K_{x_s} \times K_u \times [t_0, T] \to K_{x_f}$. Fast states x_f and slow states x_s evolve on different temporal scales, with the small parameter ϵ influencing the rate of change of x_s to be much slower than that of x_f, thus defining the time-scale separation.

Lemma 1: Given the system structure like as in Eqs. (3.8)-(3.9) with $x_f \in K_{x_f}$, $x_s \in K_{x_s}$, and $u \in K_u$, $\epsilon > 0$ small, and g, f continuously differentiable. If there exists $\delta > 0$ such that for $\|x_f - x_{f,eq}\| < \delta$ and $\|x_s - x_{s,eq}\| < \delta$, where $(x_{f,eq}, x_{s,eq})$ is an equilibrium point, then the system exhibits time-separability between x_f and x_s dynamics for $t_0 \leq t \leq T$.

Proof: Let us analyze the growth-order asymptotics of the system at some arbitrary time t_k. Assume that system distance to equilibrium is bounded as $\mathcal{O}(\|\Delta x_1\|) \leq \mathcal{O}(1)$, $\mathcal{O}(\|\Delta x_2\|) \leq \mathcal{O}(1)$, $\mathcal{O}(\|\Delta u\|) \leq \mathcal{O}(1)$, then:

$$\begin{aligned}
\mathcal{O}(\|\Delta x_s^k\|) &\approx \epsilon[\|F_{x_f}\| + \|F_{x_s}\| + \|F_u\|]\mathcal{O}(1) \\
&\leq \epsilon[\|F_x\| + \|F_z\| + \|F_u\|]\mathcal{O}(1) \\
\mathcal{O}(\|\Delta x_f^k\|) &\approx [\|G_{x_f}\| + \|G_{x_s}\| + \|G_u\|]\mathcal{O}(1) \\
&\leq [\|G_{x_1}\| + \|G_{x_2}\| + \|G_u\|]\mathcal{O}(1)
\end{aligned}$$

By ensuring $\mathcal{O}(\|F_{x_1}\|) \leq \mathcal{O}(\epsilon^{-2})$, $\mathcal{O}(\|F_{x_2}\|) \leq \mathcal{O}(\epsilon^{-2})$, and $\mathcal{O}(\|F_u\|) \leq \mathcal{O}(\epsilon^{-2})$ along with $\mathcal{O}(\|G_{x_1}\|) \leq \mathcal{O}(1)$, $\mathcal{O}(\|G_{x_2}\|) \leq \mathcal{O}(1)$, and $\mathcal{O}(\|G_u\|) \leq \mathcal{O}(1)$ one can establish bounds that imply time-separability.

Lemma 1 provides the sufficient conditions for the time-separability of the system. It specifies that if the system's state variables are sufficiently close to an equilibrium point and if the system's dynamics are continuously differentiable, then the system exhibits time-separability. This lemma essentially tells us that under these conditions, it's possible to separately analyze the fast and slow dynamics of the system, which means that subsystems are time-scale separable.

Lemma 2: Consider the system of Eqs. (3.8)-(3.9) exhibiting time-separability. Assume g, f are continuously differentiable in a neighborhood of an equilibrium point $(x_{f,eq}, x_{s,eq})$. Then, for $t_0 \leq t \leq T$ and every (x_f, x_s, u) sufficiently close to $(x_{f,eq}, x_{s,eq}, u_{eq})$, there exist constants $C_g, C_f > 0$ such that

$$\begin{aligned}
\|\nabla g(x_f, x_s, u, t)\| &\leq C_g \\
\|\nabla f(x_f, x_s, u, t)\| &\leq C_f
\end{aligned}$$

where ∇g and ∇f represent the Jacobian matrices of g and f, respectively, and $\|\cdot\|$ denotes

an appropriate matrix norm.

Proof: Similarly to Lemma 1 proof there is

$$\mathcal{O}(\|\Delta x_s^k\|) \leq \epsilon[\|F_x\| + \|F_z\| + \|F_u\|]\mathcal{O}(1)$$
$$\mathcal{O}(\|\Delta x_f^k\|) \leq [\|G_{x_1}\| + \|G_{x_2}\| + \|G_u\|]\mathcal{O}(1)$$

It follows that the system's time-separability $\mathcal{O}(\|\Delta x_1^k\|) \approx \mathcal{O}(1)$ and $\mathcal{O}(\|\Delta x_2^k\|) \approx \mathcal{O}(\epsilon)$ implies upper-bounds on Jacobians.

Lemma 2, implies that if the system exhibits time-separability, then the Jacobian matrices of the system (derived from g and f) have finite upper bounds when sufficiently close to the equilibrium. Bounded Jacobians near an equilibrium point imply that the system's response to perturbations is limited. It builds on the time-separability established by Lemma 1 and provides additional structure to the system's behavior near equilibrium.

Theorem 3: Given the multiscale system described by Eqs. (3.8)-(3.9), assume the system is sufficiently close to an equilibrium state. Then, the system exhibits time-separability if and only if the system dynamics are continuously differentiable with respect to their respective variables.

Proof: Follows directly from proofs of Lemma 1 and Lemma 2.

This theorem established that the bounded Jacobian matrices of the system Eqs. (3.8-3.9) are necessary and sufficient conditions for the time-separability. The specific bounds on the Jacobian matrices in the problem of parameter estimation can be seen through the understanding of the rate of change of the data which implies that the parameters of the system that explains the data, are bounded.

It's important to note that the interval for observing the slow system's variability must be of order $\Delta t_s = O(\epsilon^{-1})$, where ϵ is a previously established small parameter indicating the separation of time scales. Conversely, the fast scale's observational interval, Δt_z, must be shorter, $\Delta t_z \leq \Delta t_s$, and typically set as $\Delta t_s = K\Delta t_f$ with $K \in \mathbb{N}$, ensuring simultaneous observation of both scales at every Δt_s interval.

3.3 Kalman Filter Joint State-Parameter Estimation

In the context of dynamic models parameters can either be constant or vary over time. To estimate unknown parameters alongside the system's state variables, one can use the Kalman Filter (KF) framework. This is a standard method for white-box models and the system parameters can be viewed as temporal quasi-static. The assumption is that parameters

change negligibly over the timescale of interest, which can be mathematically expressed as

$$\frac{dp}{dt} \approx 0 \tag{3.10}$$

Kalman Filter inherently operates in discrete time and relies on discrete data measurements. The state-space representation of the system is augmented to include these parameters as additional states. This augmentation allows us to apply the KF for joint state and parameter estimation, and the augmented state vector at any discrete time step k is given by

$$\mathbf{x}_{a,k} = \begin{bmatrix} \mathbf{x}_k \\ \mathbf{p}_k \end{bmatrix} \tag{3.11}$$

where $\mathbf{x}_k$ represents the state variables such as position, velocity, etc., denoted $\mathbf{x}_k = [x_k, v_{x,k}, \dots]^T$, and $\mathbf{p}_k$ consists of the parameters such as mass, drag coefficient, etc., $\mathbf{p}_k = [m, b_x, T_f, \dots]^T$. The index k indicates the time step in the discrete model.

Given the estimated augmented state $\hat{\mathbf{x}}_{a,k}$ and the corresponding covariance $\hat{\mathbf{P}}_k$, the Kalman Filter updates these estimates using the linear system and measurement models at each time step. The KF algorithm comprises two main steps: prediction and update. The prediction phase projects the current state estimate and covariance forward in time

$$\mathbf{x}^-_{a,k+1} = \mathbf{F}_k \hat{\mathbf{x}}_{a,k} + \mathbf{B}_k \mathbf{u}_k \tag{3.12}$$

$$\mathbf{P}^-_{k+1} = \mathbf{F}_k \hat{\mathbf{P}}_k \mathbf{F}_k^T + \mathbf{Q}_k \tag{3.13}$$

where $\mathbf{F}_k$ is the state transition matrix representing the system dynamics, $\mathbf{B}_k$ is the control input matrix, $\mathbf{u}_k$ is the control input, and $\mathbf{Q}_k$ is the process noise covariance matrix. When a new measurement $\mathbf{y}_{k+1}$ is received, the measurement update is given by

$$\mathbf{S}_{k+1} = \mathbf{H}_{k+1} \mathbf{P}^-_{k+1} \mathbf{H}^T_{k+1} + \mathbf{R}_{k+1} \tag{3.14}$$

$$\mathbf{K}_{k+1} = \mathbf{P}^-_{k+1} \mathbf{H}^T_{k+1} \mathbf{S}^{-1}_{k+1} \tag{3.15}$$

$$\hat{\mathbf{x}}_{a,k+1} = \mathbf{x}^-_{a,k+1} + \mathbf{K}_{k+1}(\mathbf{y}_{k+1} - \mathbf{H}_{k+1} \mathbf{x}^-_{a,k+1}) \tag{3.16}$$

$$\hat{\mathbf{P}}_{k+1} = (I - \mathbf{K}_{k+1} \mathbf{H}_{k+1}) \mathbf{P}^-_{k+1} \tag{3.17}$$

where $\mathbf{H}_{k+1}$ is the observation matrix relating the state to the measurement, $\mathbf{R}_{k+1}$ is the measurement noise covariance matrix, and I is the identity matrix.

By iteratively applying these predictions and updating equations, the Kalman Filter provides real-time optimal estimation of the linear system's state and parameters, refining

its estimates with each new measurement and the system's known dynamics.

To accommodate nonlinearities in the system dynamics or the measurement model, the Extended Kalman Filter (EKF) is employed. The EKF linearizes the system around the current state estimate at each time step. The dynamics and measurement functions are denoted as $\mathbf{f}(\mathbf{x}_{a,k}, \mathbf{u}_k)$ and $\mathbf{h}(\mathbf{x}_{a,k})$, respectively. The prediction equations for the EKF are

$$\mathbf{x}_{a,k+1}^{-} = \mathbf{f}(\hat{\mathbf{x}}_{a,k}, \mathbf{u}_k)$$

$$\mathbf{P}_{k+1}^{-} = \mathbf{F}_k \hat{\mathbf{P}}_k \mathbf{F}_k^T + \mathbf{Q}_k$$

where $\mathbf{F}_k = \frac{\partial \mathbf{f}}{\partial \mathbf{x}_a}\Big|_{\hat{\mathbf{x}}_{a,k}}$ is the Jacobian of the dynamics function. Upon receiving a new measurement $\mathbf{y}_{k+1}$, the update equations are

$$\mathbf{S}_{k+1} = \mathbf{H}_{k+1} \mathbf{P}_{k+1}^{-} \mathbf{H}_{k+1}^T + \mathbf{R}_{k+1}$$

$$\mathbf{K}_{k+1} = \mathbf{P}_{k+1}^{-} \mathbf{H}_{k+1}^T \mathbf{S}_{k+1}^{-1}$$

$$\hat{\mathbf{x}}_{a,k+1} = \mathbf{x}_{a,k+1}^{-} + \mathbf{K}_{k+1}(\mathbf{y}_{k+1} - \mathbf{h}(\mathbf{x}_{a,k+1}^{-}))$$

$$\hat{\mathbf{P}}_{k+1} = (I - \mathbf{K}_{k+1}\mathbf{H}_{k+1})\mathbf{P}_{k+1}^{-}$$

where $\mathbf{H}_{k+1} = \frac{\partial \mathbf{h}}{\partial \mathbf{x}_a}\Big|_{\mathbf{x}_{a,k+1}^{-}}$ is the Jacobian of the measurement function.

Based on the previously introduced joint state-parameter estimation, system Eqs. (2.26)-(2.30) is rewritten as follows

$$\dot{x}_{\text{aug}} = \begin{bmatrix} v_x \\ v_y \\ \frac{1}{m}u_x - \frac{b_x}{m}v_x \\ \frac{1}{m}u_y - \frac{b_y}{m}v_y \\ -\alpha F_x v_x - \beta F_y v_y - \gamma P_b - \frac{1}{T_f}f \\ 0 \\ 0 \\ 0 \\ 0 \\ 0 \\ 0 \\ 0 \end{bmatrix} \tag{3.18}$$

The augmented state vector includes not only the states but also the parameters that are assumed to be constant (or vary slowly compared to states):

$$\mathbf{x}_{\text{aug}} = \Big[x, y, v_x, v_y, f, m, b_x, b_y, \alpha, \beta, \gamma, T_f\Big]^T \tag{3.19}$$

Given the presence of time-scale separation in the equation for $\dot{f}$, where v_x and v_y enter as constants ($\bar{v}_x$ and $\bar{v}_y$), the bilinear part of the system linearizes around the operating point at a slower timescale. Nevertheless, the parameters are now the part of augmented states, so EKF is used as Eq. (3.18) needs to be linearized. The vector of measurable states from drone flight mission data is:

$$\mathbf{y}_{measure} = \Big[x, y, v_x, v_y, f\Big]^T \tag{3.20}$$

The EKF is used to estimate the states and consequently parameters by predicting the next state based on the current state and the dynamics function. The update of the state prediction is based of new measurements, which in turn refines parameter estimates.

Disturbance-Aware Policy for Fuel Efficient Flight Mission

Time-critical systems have to adhere to timing constraints, which if not satisfied can lead to system and operation failure. In the pursuit of efficiency, especially in time-critical systems affected by disturbances, the theme of near-optimal composite control remains one of the central topics in control theory [19]-[20]. Drones as such systems have to manage and guarantee strict time requirements to ensure system stability, safety, and reliability. This section outlines the methodology for decomposing singularly perturbed linear systems and discusses modifications to the online policy computed using the Linear-Quadratic Regulator (LQR) in the presence of disturbances.

4.1 Singular Perturbation Decomposition of the Lateral-Fuel Flow Model

Similarly to [20], consider a singularly perturbed linear time-invariant system

$$\dot{x}_1 = A_{11}x_1 + A_{12}x_2 + B_1u, \tag{4.1}$$

$$\epsilon\dot{x}_2 = A_{21}x_1 + A_{22}x_2 + B_2u, \tag{4.2}$$

$$y = C_1x_1 + C_2x_2, \tag{4.3}$$

where ϵ is a small positive scalar, the state x is formed by the R^{n_1} and R^{n_2} vectors x_1, x_2, the control u is an R^m vector and the output y a R^k vector.

The system of Eqs. (4.1-4.3) is characterized by a two-time-scale property, with n_1 eigenvalues of small magnitude $\mathcal{O}(1)$ and n_2 eigenvalues having large magnitude $\mathcal{O}(1/\epsilon)$. Before achieving a bifurcation of slow and fast dynamics, system Eq. (4.1) undergoes an approximate decomposition into a slow subsystem comprising n_1 small eigenvalues and a fast subsystem with n_2 large eigenvalues. Within an asymptotically stable regime, the system's

transient behavior is predominantly governed by the fast modes associated with the large eigenvalues. After the transient phase, these modes become negligible, and the system's dynamics are predominantly attributed to the slow modes. An assumption of infinitely fast modes, i.e., $\epsilon \to 0$ in Eq. (4.1), essentially cancels their influence, thus simplifying system Eq. (4.1) to

$$\dot{x}_1 = A_{11}x_1 + A_{12}\bar{x}_2 + B_1 u,\ x_1(0) = \bar{x}_{10} \tag{4.4}$$

$$0 = A_{21}x_1 + A_{22}\bar{x}_2 + B_2 u \tag{4.5}$$

$$\bar{y} = C_1 x_1 + C_2 \bar{x}_2 \tag{4.6}$$

Overbar denotes the slow part of all respective variables when $\epsilon = 0$. Under assumption of A_{22} to be invertible, $\bar{x}_2$ is expressed as

$$\bar{x}_2 = -A_{22}^{-1}(A_{21}\bar{x}_1 + B_2\bar{u}) \tag{4.7}$$

Substituting into (2), the slow subsystem of (1) is thus defined as:

$$\dot{x}_s = A_0 x_s + B_0 u_s,\ x_s(0) = x_{1,0} \tag{4.8}$$

$$y_s = C_0 x_s + D_0 u_s \tag{4.9}$$

where $x_s = \bar{x}_1$, $y_s = \bar{y}_1$, $u_s = \bar{u}$ and

$$A_0 = A_{11} - A_{12}A_{22}^{-1}A_{21}, \qquad B_0 = B_1 - A_{12}A_{22}^{-1}B_2,$$
$$C_0 = C_1 - C_2 A_{22}^{-1}A_{21}, \qquad D_0 = -C_2 A_{22}^{-1}B_2.$$

To obtain the fast subsystem, the assumption is that the slow variables remain invariant during transients of the fast subsystem, implying $\dot{\bar{x}}_2 = 0$ and $x_1 = \bar{x}$, are constant. Integrating these conditions into Eqs. 4.2 and 4.3, one obtains

$$\epsilon\dot{x}_f = A_{22}x_f + B_2 u_f,\ x_f(0) = x_{2,0} - \bar{x}_2(0) \tag{4.10}$$

$$y_f = C_2 x_f \tag{4.11}$$

where $x_f = x_2 - \bar{x}_2$, $u_f = u - \bar{u}$, and $y_f = y - \bar{y}$ and thus, defining the fast subsystem.

As the state variables of system Eqs. (2.26)-(2.30) are fully observable, one can see coming from the data difference in magnitude of change of state variables. An analysis of the dynamic behavior of a system will focus on the consecutive state magnitude change and the corresponding volatility. Volatility is defined here as the standard deviation of the first

difference of each variable of the states over the measured time period. It represents the average rate at which each variable's rate of change fluctuates over the entire trajectory. Volatility quantifies the average variability of the rate of change 4.2 and indicates the relative change of each variable over time. The Fig. 4.1 supports time-scale separation as one can see how consecutive state magnitude changes. This is computed as the absolute differences between the consecutive data points, to highlight moments where significant shifts in dynamics occur. The results indicate that v_x and v_y exhibit higher volatility and more frequent and pronounced spikes in their changes compared to f, suggesting faster and more reactive dynamics. Conversely, f displays lower volatility and fewer spikes, indicating slower dynamics and a more gradual response to system changes.

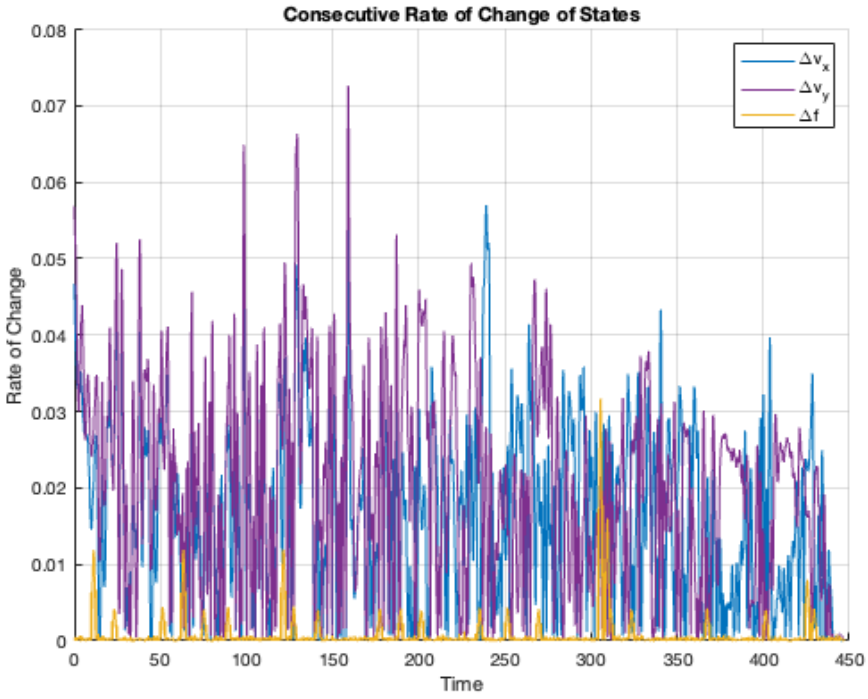

Figure 4.1: Consecutive Rate of Change of States

Under the influence of $d_f(t)$ which is a battery-bound disturbance $|d_f(t)| \leq D, \forall t \leq T$,

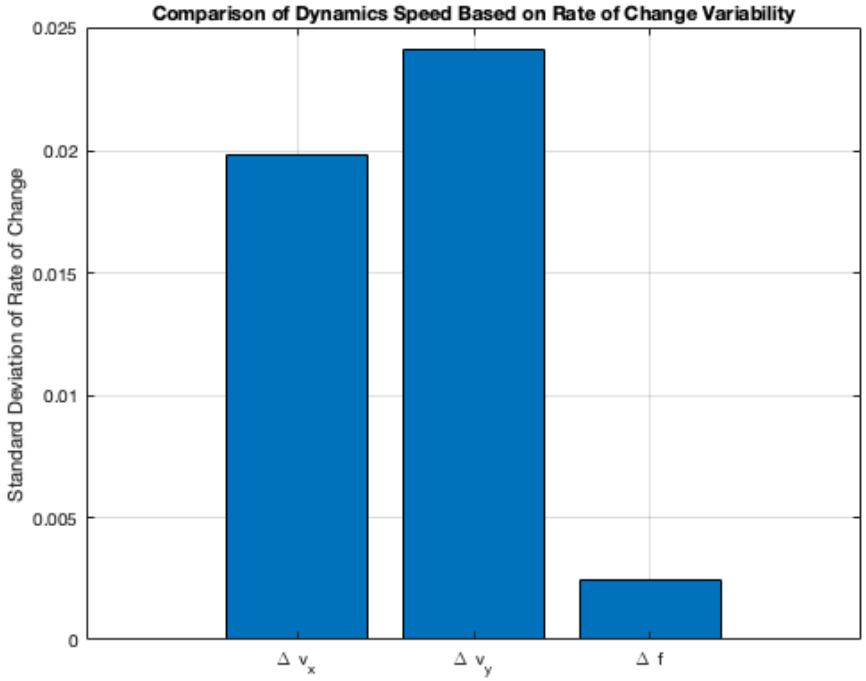

Figure 4.2: Comparison of Dynamics Speed Based on Rate of Change Variability

where T is the time horizon of the flight. The system (2.26)-(2.30) can be rewritten as

$$\dot{x} = v_x, \qquad x(0) = x_0 \tag{4.12}$$

$$\dot{y} = v_y, \qquad y(0) = y_0 \tag{4.13}$$

$$\dot{v}_x = \frac{1}{m}u_x - \frac{b_x}{m}v_x, \qquad v_x(0) = v_{x,0} \tag{4.14}$$

$$\dot{v}_y = \frac{1}{m}u_y - \frac{b_y}{m}v_y, \qquad v_y(0) = v_{y,0} \tag{4.15}$$

$$\dot{f} = -\alpha u_x v_x - \beta u_y v_y - \gamma d_f - \frac{1}{T_f}f \qquad f(0) = f_0 \tag{4.16}$$

For the system 4.12-4.15 due to the time-scale separation, one can observe that the slow subsystem becomes a linear model as $\epsilon \to 0$ as from the fast subsystem (4.12)-(4.15) it follows

$$\overline{v}_x = \frac{u_x}{b_x} \tag{4.17}$$

$$\overline{v}_y = \frac{u_y}{b_y} \tag{4.18}$$

as the timescale becomes stretched $O(t/\epsilon) \to O(\tau)$ due the property of the timescale sepa-

ration. Based on previous data based argument on separate timescale dynamics

$$\underbrace{\dot{f}}_{\dot{x}_1} = \underbrace{-\frac{1}{T_f}}_{A_{11}} f + \underbrace{\begin{bmatrix}\alpha\bar{v}_x & \beta\bar{v}_y\end{bmatrix}}_{B_1}\begin{bmatrix}u_x\\u_y\end{bmatrix} - \gamma d_f, \qquad f(0) = f_0 \tag{4.19}$$

$$\underbrace{\begin{bmatrix}\dot{v}_x\\\dot{v}_y\end{bmatrix}}_{\dot{x}_2} = \underbrace{\begin{bmatrix}-\frac{b_x}{m} & 0\\0 & -\frac{b_y}{m}\end{bmatrix}}_{A_{22}}\begin{bmatrix}v_x\\v_y\end{bmatrix} + \underbrace{\begin{bmatrix}\frac{1}{m} & 0\\0 & \frac{1}{m}\end{bmatrix}}_{B_2}\begin{bmatrix}u_x\\u_y\end{bmatrix}, \qquad \begin{bmatrix}v_x(0)\\v_y(0)\end{bmatrix} = \begin{bmatrix}v_{x,0}-\overline{v}_x\\v_{y,0}-\overline{v}_y\end{bmatrix} \tag{4.20}$$

$$\underbrace{\begin{bmatrix}f\\v_x\\v_y\end{bmatrix}}_{y} = \underbrace{\begin{bmatrix}1\\0\\0\end{bmatrix}}_{C_1}\begin{bmatrix}f\end{bmatrix} + \underbrace{\begin{bmatrix}0 & 0\\0 & 1\\0 & 1\end{bmatrix}}_{C_2}\begin{bmatrix}v_x\\v_y\end{bmatrix} \tag{4.21}$$

where Eqs. (2.26)-(2.27) can be obtained from x_2 subsystem through integration. The system Eqs. (4.19)-(4.21) can now be timescale separated, where $A_{12} = A_{21} = 0$. Disturbance in (4.19) can be transformed as input. From here on, as there is no coupling between x_1 and x_2 the slow dynamics of the system can be rewritten as $x_s = f$:

$$\dot{x}_s = A_0 f + B_0 u_s - \gamma d_f, \qquad x_s(0) = x_{1,0} \tag{4.22}$$

$$y_s = C_0 x_s + D_0 u_s \tag{4.23}$$

and and $D_0 = 0$. Meanwhile, fast dynamics $x_f = [v_x\ v_y]^T$ is

$$\epsilon\dot{x}_f = A_{22}x_f + B_2 u_f, \qquad x_f(0) = x_{2,0} - \overline{x}_2(0) \tag{4.24}$$

$$y_f = C_2 x_f \tag{4.25}$$

where ϵ is the system mass m.

4.2 Near-Optimal Composite Powertrain Regulation

The optimal state regulator problem for system Eqs. (4.12)-(4.15) and its respective cost function or performance index, that is to be minimized

$$J = \frac{1}{2}\int_0^\infty (y^\top y + u^\top R u)\, dt \tag{4.26}$$

$$s.t.\ \textbf{Eq.}\ 4.1 - 4.3 \tag{4.27}$$

is after timescale decomposition divided into two separate regulation problems corresponding to the slow and fast subsystems. By extracting two quadratic performance indices from J, one tailored to the dynamics of the slow subsystem as shown in Eqs. (4.28), and the other subject to the fast subsystem dynamics as in Eqs. (4.33), a solution from two separate regulation problems can be established. These are referred to as the slow dynamics subsystem problem and the fast dynamics subsystem problem. The optimal control solutions u_s and u_f for each subsystem lead to the formation of a composite control $u_c = u_s + u_f$, designed for implementation on the original system (4.12)-(4.15). The results and performance of this composite regulation will be shown in the Chapter 5.4.

Slow Dynamics Problem

The problem is to find u_s to minimize

$$J_s = \frac{1}{2}\int_0^\infty (y_s^T Q_s y_s + u_s^T R_s u_s)\, dt, \tag{4.28}$$

$$s.t.\ \textbf{Eqs}.\ 4.22 - 4.23 \tag{4.29}$$

for the slow subsystem Eq. (4.22)-(4.23) where both Q_s, R_s are positive semi-definite.

Regarding x_s and u_s, cost function (4.28) becomes

$$J_s = \frac{1}{2}\int_0^\infty \left[x_s^T C_0^T Q_s C_0 x_s + 2u_s^T D_0^T C_0 x_s + u_s^T R_0 u_s\right] dt, \tag{4.30}$$

where $R_0 = R_s + D_0^T D_0$.

From [21] it follows that u_s is equal to

$$u_s = -R_0^{-1}(D_0 C_0 + B_0 K_s) x_s \tag{4.31}$$

where K_s is a positive semidefinite stabilizing solution of LQ problem Eq. (4.28)

$$K_s = lqr(A_0, B_0, Q_s, R_s) \tag{4.32}$$

Fast Dynamics Problem

For the fast dynamics problem, the objective is to find u_f to minimize

$$J_f = \frac{1}{2}\int_0^\infty (y_f^T Q_f y_f + u_f^T R_f u_f), dt \tag{4.33}$$

$$s.t. \textbf{ Eqs. } (4.24) - (4.25) \tag{4.34}$$

where both Q_f, R_f are positive semi-definite and for the linearized fast subsystem Eqs. (4.24-4.25) dynamics of the optimal control u_f is

$$u_f = -R^{-1} B_2 K_f x_f \tag{4.35}$$

where K_f is the positive semidefinite stabilizing solution of minimization of Eq. 4.33

$$K_s = lqr(A_{22}, B_2, Q_f, R_f) \tag{4.36}$$

Control Algorithm Pseudo-Code

As is outlined in psuedo-code of Alg. 1, there is a set of predefined parameters that includes $R > 0$, A_s, A_f, B_s, B_f, Q_s, and Q_f. These parameters are important in shaping the system's dynamics and establishing control objectives. The control depends on iteratively solving for the control inputs $u_s(t)$ and $u_f(t)$, corresponding to the slow and fast subsystems. This iterative process involves the minimization of the respective cost functions J_s and J_f. These cost functions, 4.28 and 4.33, are subject to the continuous dynamics of the system, described by Eqs. (4.22-4.23) and Eqs. (4.24-4.25), accordingly. Upon obtaining the optimal control inputs $u_s(t)$ and $u_f(t)$, the algorithm sums them and generates composite control $u_c(t) = u_s(t) + u_f(t)$. This control is then applied to the original system Eqs. (4.1-4.3), enabling computationally simplified management of the system's multi-rate dynamics. The states x_s and x_f and the cost functions J_s and J_f are updated continuously to ensure that the control inputs are optimally aligned with the evolving state of the system. The algorithm proceeds until it reaches the end of the specified time horizon, resulting in the trajectory of optimized $u_c(t)$ that balances the regulation of both the slow and fast system dynamics.

The control is calculated based of continuous dynamics with discrete time step ΔT which will be chosen depending on the sampling time of the measurements y_f.

Algorithm 1 Near-Optimal Composite Regulation in Discrete Time

Initialize parameters: A_s, A_f, B_s, B_f, Q_s, Q_f, R_s, R_f
Initialize: x_{s0}, x_{f0}, $J_s = J_f = 0$, $t = 0$
while $t < T$ **do**
    Solve for discrete control $u_s[k]$ optimizing
    $J_s = \frac{1}{2}\sum_{k=0}^{\infty}(y_s[k]^\top Q_s y_s[k] + u_s[k]^\top R u_s[k])\Delta T$
        subject to $x_s[k+1] = A_s x_s[k] + B_s u_s[k]$
    Solve for discrete control $u_f[k]$ optimizing
    $J_f = \frac{1}{2}\sum_{k=0}^{\infty}(y_f[k]^\top Q_f y_f[k] + u_f[k]^\top R u_f[k])\Delta T$
        subject to $x_f[k+1] = A_f x_f[k] + B_f u_f[k]$
    Form composite control $u_c[k] = u_s[k] + u_f[k]$
    Apply $u_c[k]$ to the original system, updating states $x_s[k+1]$, $x_f[k+1]$ for the next step
    Increment t by a time-step ΔT
end while
Output: Optimized composite control policy $u_c[k]$ over discrete intervals from 0 to T

4.3 Disturbance Aware Composite Policy

The disturbance doesn't show up in the fast subsystem and for the slow subsystem, as it is affected by a battery disturbance, the slow control $u_s = [u_{x,s}, u_{y,s}]^T$ can be either blind or aware of such disturbance. The fast system computed control $u_f = [u_{x,f}, u_{y,f}]^T$ will always be blind towards battery disturbance. In this section I'll introduce how one can compute disturbance aware control following on the recent research findings.

Suppose, like in [22] that each of the previously defined linearly invariant slow and fast subsystems Eqs. (4.8)-(4.11) can be discretized and in the following LTI form

$$x_{t+1} = Ax_t + Bu_t + d_t, \quad t = 0, 1, \ldots, T-1, \tag{4.37}$$

where $A \in \mathbb{R}^{n\times n}$ is system state and $B \in \mathbb{R}^{n\times m}$ is system input matrix, $x_t \in \mathbb{R}^n$ is the system state and $u_t \in \mathbb{R}^m$ is the control input, while $d_t \in \mathbb{R}^n$ is an external disturbance, and T is the time horizon over which the system is controlled. Thefocus is on the situations where the disturbances d_t are sparse $d_t \neq 0$ if and only if $t \in D$, for some index set $D = \{t_1, t_2, \ldots, t_{|D|}\}$, where $|D|$ denotes the set cardinality of D. The nonzero disturbances are given by $d_k = w_k$, $k \in 1, \ldots, |D|$, and are bounded in ℓ_2 norm by $\|w_k\| \leq W \ \forall k$.

The objective of online policy is to minimize the cost

$$\mathop{\mathbb{E}}_{d_0,\ldots,d_{T-1}} \left(x_T^T Q_T x_T + \sum_{t=0}^{T-1} x_t^T Q x_t + u_t^T R u_t \right) \tag{4.38}$$

where $Q_T, Q \in \mathbb{R}^{n\times n}$ are positive semi-definite and $R \in \mathbb{R}^{m\times m}$ is positive definite matrix.

When disturbances are disregarded $d = 0, \forall t \in [t_0, T]$, the conventional LQR control policy assumes a disturbance-free environment, a simplification that may not be aligned with reality. Our assumption is that disturbances d are independent with a zero mean. The optimal disturbance-free policy becomes an LQR controller [23] of the form $u_t = -K_t x_t$, for $t = [0 \dots T)$, where

$$K_t = (B^\top P_{t+1} B + R)^{-1} B^\top P_{t+1} A \tag{4.39}$$

and the sequence P_t arises from solving the discrete-time Riccati equation

$$P_t = A^\top \left(P_{t+1} - P_{t+1} B (B^\top P_{t+1} B + R)^{-1} B^\top P_{t+1} \right) A + Q \tag{4.40}$$

with $P_T = Q_T$.

Moving to a scenario where the optimal policy knows the disturbance d_t, the structure of optimal control is modified following the recent result [24]. Under the assumption that the control has complete knowledge (or reliably can predict) of all disturbances $d(t)$, $\forall t \in [t_0, T]$, the optimal policy and cost have the following structure

$$\begin{aligned}
u_t^* &= -K_t x_t - (B^\top P_{t+1} B + R)^{-1} \\
&\quad \times B^\top (P_{t+1} d_{t+1} + \frac{1}{2} v_{t+1}), && (4.41)\\
V_t(x) &= x^\top P_t x + v_t^\top x + q_t, && (4.42)\\
v_t &= 2A^\top S_t d_t + A^\top S_t P_{t+1}^{-1} v_{t+1}, && (4.43)\\
q_t &= q_{t+1} + d_t^\top S_{t+1} d_t + v_{t+1}^\top P_{t+1}^{-1} S_t d_t \\
&\quad - \frac{1}{4} v_{t+1}^\top B (B^\top P_{t+1} B + R)^{-1} B^\top v_{t+1}, && (4.44)\\
S_t &:= P_{t+1} - P_{t+1} B (B^\top P_{t+1} B + R)^{-1} B^\top P_{t+1}, && (4.45)
\end{aligned}$$

where $V_t(x)$ represents the cost-to-go of a state x at time t, and $v_t \in \mathbb{R}^n$, $q_t \in \mathbb{R}$ are recurrences that depend only on the noise d_t and are initialized to $v_T = 0$, $q_T = 0$. The optimal control is determined by the optimal online policy action and a second term depending exclusively on future disturbances.

Control Algorithm Pseudo-Code

The algorithm 2 which optimizes system performance under stochastic disturbances and integrates the dynamics of the altitude-fuel flow system. The algorithm begins with the system's

initial state $x(0)$ and employs a predictive function $d(v_z(t), v_w(t))$ for anticipating wind disturbances, essential for disturbance-aware control strategies. This predictive approach allows the algorithm to proactively adjust to environmental changes. At each step, the algorithm resolves a discrete-time optimization problem within the moving horizon $[t, t + \Delta t]$, aiming to minimize the objective function defined by:

$$\sum_{\tau=t}^{t+\Delta t} \left(x(\tau)^\top Q x(\tau) + u(\tau)^\top R u(\tau) \right) \Delta t,$$

which balances system performance against energy conservation through optimal state regulation and control effort. The predictive modeling of disturbances is critical for a responsive and adaptive control system. Upon computing the optimal control $u^*(t)$, the control is applied to the system, advancing the timeframe by Δt. The control law is continuously updated through this iterative process. The procedure culminates in the generation of an optimal control trajectory $u^*(t)$ over the period $[0, T)$.

Algorithm 2 Near-Optimal Composite Regulation with Disturbance Awareness

1: Initialize parameters: A_s, A_f, B_s, B_f, Q_s, Q_f, R_s, R_f
2: Initialize: x_{s0}, x_{f0}, $J_s = J_f = 0$, $t = 0$, $d_t = 0$
3: **while** $t < T$ **do**
4: Predict and update battery disturbance d_t for the slow subsystem
5: Solve for discrete control $u_s[k]$ optimizing:

$$J_s = \frac{1}{2} \sum_{k=t}^{t+\Delta T} \left(y_s[k]^\top Q_s y_s[k] + u_s[k]^\top R u_s[k] \right)$$

subject to $x_s[k+1] = A_s x_s[k] + B_s u_s[k] + d_t$
6: For the fast subsystem, solve for discrete control $u_f[k]$ optimizing:

$$J_f = \frac{1}{2} \sum_{k=t}^{t+\Delta T} \left(y_f[k]^\top Q_f y_f[k] + u_f[k]^\top R u_f[k] \right)$$

subject to $x_f[k+1] = A_f x_f[k] + B_f u_f[k]$
7: Form composite control $u_c[k] = u_s[k] + u_f[k]$
8: Apply $u_c[k]$ to the original system, updating states $x_s[k+1]$, $x_f[k+1]$ for the next step
9: Increment t by a time-step ΔT
10: **end while**
11: **Output:** Optimized composite control trajectory $u_c[k]$ over discrete intervals from 0 to T

Decentralized Information Exchange for Improved Fuel Savings

5.1 Modular Energy Modeling of Interconnected Systems

In modeling interconnected systems, it is necessary to use a framework that supports both detailed local analysis and provides a holistic system understanding. This approach is particularly appealing in systems like hybrid powertrain drones, where different power sources, loads, and energy conversions must be controlled at the same time. Previous research ([14], [25]) has emphasized the benefits of an energy-based modular modeling approach, which allows for dynamic simulation and control through local interactions within subsystems and across the system as a whole or essentially through tearing, zooming, and linking [26]. Unlike models that often decouple information exchange effects from control signals, the interactive information exchange is modeled maintaining the interconnection of the system without this simplification, providing a more intuitive and comprehensive representation of system behavior.

5.1.1 Integrated Physical, Information, and Control Layers in Energy-Efficient Hybrid Powertrain Systems

The hybrid drone powertrain system consists of different multi-domain physical subsystems. This complex interconnected system integrates a fuel reservoir, a fuel engine, and a generator with a battery, and each component can be viewed through the lens of physical, information exchange, and control layers. Each layer can be considered in isolation and as components shouldn't be viewed separately, these layers, particularly information and control shouldn't be separated. An accurate representation of each subsystem model is important for optimizing powertrain energy efficiency and improving drone performance without destabilizing other components through interconnected interactions [27].

Physical Layer

The hybrid drone powertrain system's physical layer comprises physical interconnected components, Fig. 2.1, that are controlled indirectly by control signals that come from FCU. At its foundation is the fuel reservoir, which supplies the fuel engine with a consistent fuel flow to convert chemical energy into mechanical power, ensuring sustained operation. This mechanical power drives a generator that converts it to electrical energy. The generator, which typically produces three-phase AC, requires an inverter to convert this output into DC suitable for powering other components. Part of this power from the inverter is directed to the battery system, which stores electrical energy and manages charge-discharge cycles, supplementing power to the powertrain when necessary to maintain optimal state-of-charge levels under various flight conditions. Simultaneously, power electronics coordinate energy flow between the generator, battery, and electric motor, ensuring efficient power distribution and conversion while adhering to control policies. This interconnected system works cohesively to achieve efficient power output, providing thrust power via the powertrain main bus while adjusting dynamically to real-time flight demands.

Information Exchange Layer

Another interpretation of the hybrid drone powertrain system is that the physical layer functions as a network of locally connected information flows, where each component continuously exchanges "data" with physically connected neighbors. What is meant by the "data" is the real power and rate of change of reactive power computed through the physical variable at the interface of each component. The fuel reservoir directly influences the fuel engine by providing a steady supply of fuel which can be interpreted as the flow of real power and rate of change of generalized reactive power, ensuring the engine can convert chemical energy into mechanical power. The fuel engine, in turn, provides demand power flow and rate of reactive power to the reservoir in which the information feedback on fuel consumption rates has been created, which then helps regulate the reservoir's output. The fuel engine drives the generator, and both components exchange power flows and rate of power on mechanical power input and electrical power output, influencing each other's performance. The generator, which generates three-phase AC, interfaces with an inverter to convert its output to DC. This inverter manages information exchange with the generator to ensure stable conversion while also providing real power and rate of reactive power to downstream components. The battery system receives the physical information from the generator, storing it while simultaneously exchanging information with the generator and power electronics to coordinate charge-discharge cycles. This allows the battery to supplement power to the powertrain,

influencing generator operations by providing power and change of reactive power on optimal energy storage levels. Power electronics plays a critical role in directing energy flows between the generator, battery, and electric motor, facilitating efficient power distribution. This electronic system collects and distributes information across the powertrain, ensuring that control signals accurately reflect real-time power needs and that the system maintains a balanced operation. In this way, the powertrain system achieves efficient, adaptive energy output, with each component continuously adjusting its operations based on information received from neighboring subsystems.

Control Layer

In the hybrid drone powertrain system's control layer, the information flow operates under a unidirectional, hierarchical framework, where each downstream component sends signals that reflect needed power. These signals propagate upstream, finally reaching the fuel reservoir, which implicitly responds to the linear combination of downstream power demand. This hierarchical communication pattern causes each component to regulate itself against others, potentially leading to non-cooperative control as components try to counteract disturbances stemming from other components. From Fig. 2.1, the fuel reservoir supplies the ICE with a steady flow of fuel to maintain a stable mechanical power output. The fuel engine receives power setpoint from the downstream generator and adjusts its operations accordingly to meet those demands. The generator, driven by the ICE, produces electrical power based on the demand set by the inverter, which converts the generator's AC output into a stable DC supply. This DC supply serves the battery system, which manages its charge-discharge cycles and signals upstream components about optimal power levels needed to supplement the powertrain efficiently. Throughout this process, each subsystem seeks to maintain its operational integrity while minimizing the effects of disturbances from other components. For instance, the generator might reject fluctuations in mechanical input by dynamically regulating its AC output or the battery system might limit discharging under certain conditions to maintain the desired state of charge. In this way, the powertrain control layer promotes self-regulation of each subsystem, with each striving to fulfill power requirements while preventing destabilization due to external interactions. Due to this system view, they can't achieve true cooperation and maximize efficiency. One approach to achieve system-wide maximum efficiency is proposed in this work by embedding control information into interaction variables that are bidirectionally exchanged.

5.2 Decentralized Interactive Flow of Information

Interaction variables were first introduced in [28]. Their use is well described in [14] and [29]. These variables preserve the structural richness essential for system control and stability analysis [30] and are the function of local variables. Each component within the interconnected system communicates through a designated interaction port, where interactions are classified either as outputs ('out') from internal energy conversions or as inputs ('in') from external system interactions. This distinction becomes critical when components are interconnected as it accounts for the causality and improves ways to analyze and control complex interconnected systems. At certain time scales it is important to take into account the impact of the flow of information in the real-time critical systems.

Stand-alone Interactive Model of a Component

The general unified energy-based aggregate model distinguishes between the incoming and outgoing interaction variables, as previously stated, and the dynamical interaction model in its general form is expressed as

$$\dot{E}_i = -\frac{E_i}{\tau_i} + P_{r_i} + P_{u_i} + P_{m_i} = p_i \tag{5.1}$$

$$\dot{p}_i = 4E_{t_i} + 2\dot{Q}_{C_i} - \dot{Q}_{r_i} - \dot{Q}_{u_i} - \dot{Q}_{m_i} \tag{5.2}$$

where $E_i,\ p_i,\ \dot{p}_i$ is stored energy, rate of change of stored energy, and acceleration of stored energy. The variable E_{t_i} is the stored energy in tangent space and τ_i is the time-constant of stored energy related to component internal dissipation. Real powers $P_{r_i}, P_{u_i}, P_{m_i}$ are interface port power, input power, and internal disturbance measured real power. Generalized reactive rate of change of powers $\dot{Q}_{C_i}, \dot{Q}_{r_i}, \dot{Q}_{u_i}, \dot{Q}_{m_i}$ are generalized internal capacitive element power, interface port power, input power, and internal disturbance measured rate of change of generalized reactive power.

Denoting the aggregate dynamical energy variables as

$$x_{z,i} = \begin{bmatrix} E_i \\ p_i \end{bmatrix}^T,$$

and the interactions with the rest of the system at local control ports, disturbance ports,

and the interconnection interface as

$$\dot{z}_{u_i} = \begin{bmatrix} P_{u_i} \\ \dot{Q}_{u_i} \end{bmatrix}^T, \dot{z}_{m_i} = \begin{bmatrix} P_{m_i} \\ \dot{Q}_{m_i} \end{bmatrix}^T, \dot{z}_{r_i} = \begin{bmatrix} P_{r_i} \\ \dot{Q}_{r_i} \end{bmatrix}^T,$$

respectively, one can see that the aggregate energy space model is linear in energy space variables. Aggregate interaction model in vector form is rewritten as

$$\dot{x}_{z,i} = A_{z,i}x_{z,i} + B_t E_{t,i} + B_z(\dot{z}_{r_i} + \dot{z}_{u_i} + \dot{z}_{m_i}) \tag{5.3}$$

where

$$B_t = \begin{bmatrix} 0 & 4 \end{bmatrix}, \quad B_z = \begin{bmatrix} 1 & -1 \end{bmatrix}$$

are consistent for any component, and the matrix

$$A_{z,i} = \begin{bmatrix} 0 & -1/\tau_i \\ 0 & 0 \end{bmatrix}$$

depends only on the time constant. Finally, the model state-space formulation is as follows

$$\dot{x}_{z,i} = A_{z,i}x_{z,i} + B_t E_{t,i} + B_z(\dot{z}_i^{r,\text{out}} + \dot{z}_i^m + \dot{z}_i^u), \qquad x_{z,i}(0) = z_{z,i0} \tag{5.4}$$

The model's closed-loop formulation simplifies to

$$\dot{x}_{z,i} = A_{\text{cl}}^{z,i}x_{z,i} + B_t E_{t,i} + B_z \dot{z}_{r,\text{out}}^i, \qquad x_{z,i}(0) = z_{z,i0} \tag{5.5}$$

The closed loop creates a change in the time constant τ_i influenced by the internal control logic.

The component is shown in Fig. 5.1 with the aggregate model layer and a conventional internal component dynamics layer. The lower-layer models compute the outgoing interaction variables $\dot{z}_i^{r,\text{out}}$, which will then be used by the upper-layer energy dynamics of the component. The incoming interaction variables from the grid, $\dot{z}_i^{r,\text{in}}$, are processed by the lower-layer models to evaluate the extended state trajectories $[x_i, r_i]$, given their initial conditions [14]

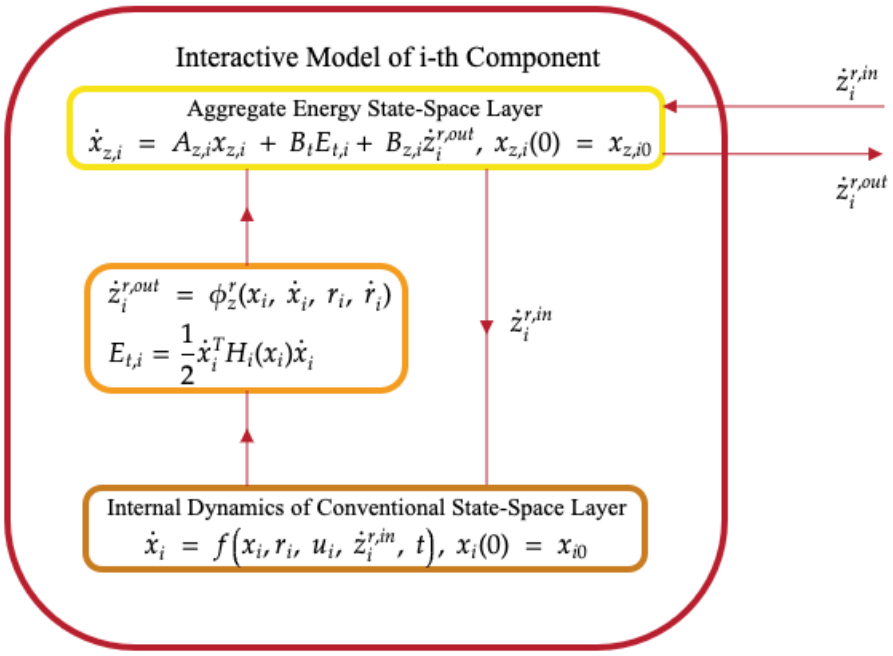

Figure 5.1: The interactive stand-alone model of a closed-loop component i

Dynamics at the Interaction Ports

At the interaction ports, where the effort variable is r_i and the flow variable is w_i^r (and based on [14] definitions 2.5 and 2.6), one can define

$$\dot{P}_i^{r,\text{in}} = r_i \frac{dw_i^r}{dt} + w_i^r \frac{dr_i}{dt} \tag{5.6}$$

$$\dot{Q}_i^{r,\text{in}} = r_i \frac{dw_i^r}{dt} - w_i^r \frac{dr_i}{dt} \tag{5.7}$$

If the flow variable is effectively the port state variable, the dynamics of the voltage can be linked to incoming disturbances $\dot{z}_i^{r,\text{in}}$ as:

$$\frac{dr_i}{dt} = \frac{1}{2w_i^r}(\dot{P}_i^{r,\text{in}} - \dot{Q}_i^{r,\text{in}}) \tag{5.8}$$

Alternatively, if the effort variable is a port state variable, the dynamics of current at the interface can be expressed by switching the negative sign in the above equation to a positive. This adjustment is essential as it allows the model to incorporate dynamic port inputs, thus acknowledging the time-varying nature of incoming interactions with the rest of the system.

Information exchange and control

The outgoing interaction variables, which result from internal energy conversion processes and interact with neighboring components, are formally defined as

$$\dot{z}_i^{r,\text{out}} = \begin{bmatrix} \int_0^t \dot{P}_i^{r,\text{out}}(s)ds \\ \dot{Q}_i^{r,\text{out}}(t) \end{bmatrix} \tag{5.9}$$

where each component of interaction variable is computed as

$$P_i^{r,\text{out}} = p_i - P_i^u - P_i^m + E_i\tau_i \tag{5.10}$$

$$Q_i^{r,\text{out}} = \int_0^t \left(-\dot{p}_i - \dot{Q}_i^u - \dot{Q}_i^m + 4E_{t,i}\right) dt \tag{5.11}$$

Based of definition of interaction variable [30], their computation can be abstracted by the following mapping

$$\dot{z}_i^{r,\text{out}} = \phi_{z,i}(x_i, \dot{x}_i, u_i, \dot{u}_i, m_i, \dot{m}_i) \tag{5.12}$$

Outgoing Interaction Variables for Components with Internal "Capacitive" Property

The definitions in Eq. 5.11 apply to purely "inductive" subsystems. In the context of systems theory, particularly in multi-domain scenarios, inductive and capacitive elements can be understood through the concepts of effort and flow variables. Inductive elements are characterized by their relationship between flow variables (like current in electrical systems or velocity in mechanical systems) and the accumulation of an effort variable (like voltage across an inductor or force in a mass). Inductance, therefore, symbolizes a resistance to changes in flow. Capacitive elements, on the other hand, are characterized by their direct storage of an effort variable which then influences the flow variable. Capacitance in a system represents the capacity to store potential (like electrical charge in capacitors or displacement in springs), and it directly responds to changes in effort variables. For subsystems containing both inductive and capacitive elements, the outgoing interaction variable element of reactive power rate is computed as

$$Q_i^{r,\text{out}} = \int_0^t \left(-\dot{p}_i - \dot{Q}_i^u - \dot{Q}_i^m + 4E_{t,i} + 2\dot{Q}_i^c\right) dt \tag{5.13}$$

Here, Q_i^c represents the reactive power absorption of capacitive components within component i.

In multi-domain systems, concepts of "inductive" and "capacitive" elements extend be-

yond electrical to include mechanical, thermal, and other types of energy storage and transformation systems. As an instance, a spring can be seen as a mechanical capacitor and a mass as a mechanical inductor. The interplay between these elements, as they send and receive energy or information through interaction variables, defines the dynamic behavior of complex systems.

Incoming Interaction Variables

The incoming interaction variables, which depend on the connection of the component with the rest of the system, are denoted as:

$$\dot{z}_i^{r,\text{in}} = \begin{bmatrix} P_i^{r,\text{in}} \\ \dot{Q}_i^{r,\text{in}} \end{bmatrix} \tag{5.14}$$

These are defined based on change of the effort and flow variables due to interconnection interaction with component port

$$P_i^{r,\text{in}} = r_i w_r^i \tag{5.15}$$

$$Q_i^{r,\text{in}} = \int_0^t \left(r_i \frac{dw_i^r}{dt} - \frac{dr_i}{dt} w_i^r \right) dt \tag{5.16}$$

Here, r_i is the port input as defined in the conventional space model, and w_r^i is the associated dual variable, which is a subset of the local state variables.

The distinction between incoming and outgoing interaction variables is important for constructing interconnected interactive models.

5.3 Interactive Energy-Based Interconnection Model

This section elaborates on the interactive energy-based interconnection model, integrating real and reactive power rate vectors from all components in the system:

$$\dot{z}_P^{r,\text{out}} = [\ldots, P_i^{r,\text{out}}, \ldots, P_j^{r,\text{out}}, \ldots]^T \tag{5.17}$$

$$\dot{z}_Q^{r,\text{out}} = [\ldots, \dot{Q}_i^{r,\text{out}}, \ldots, \dot{Q}_j^{r,\text{out}}, \ldots]^T \tag{5.18}$$

Similarly, the incoming interaction variables are defined as vectors $\dot{z}_{\text{in}}^P$ and $\dot{z}_{\text{in}}^Q$. Each outgoing interaction variable is computed individually by its respective component, while incoming interaction variables result from the system interconnection. The dynamical interconnection

relations in the $E-P$ space are given by:

$$\dot{z}_P^{r,\text{in}} = L_z \dot{z}_P^{r,\text{out}} \tag{5.19}$$

$$\dot{z}_Q^{r,\text{in}} = L_z \dot{z}_Q^{r,\text{out}} \tag{5.20}$$

where the elements of L_z are $L_{z_{ij}} = -1$ if components i and j are directly connected, otherwise zero. This forms a non-singular sparse matrix preserving the system's structure. For a single component, the relation simplifies to:

$$\dot{z}_i^{r,\text{in}} = -\sum_{j \in \mathcal{C}_i} \dot{z}_j^{r,\text{out}} \tag{5.21}$$

where $\mathcal{C}_i$ denotes the set of neighboring components of component i. This results in a higher-layer interconnected system model described by the following ODE's in aggregated interactive energy $E-P$ space for $\mathcal{N}$ connected components

$$\dot{x}_{z,i} = A_{\text{cl}}^{z,i} x_{z,i} + B_t E_{t,i} + B_z \dot{z}_{r,\text{out}}^i, \qquad x_{z,i}(0) = z_{z,i0} \quad \forall i \in \mathcal{N} \tag{5.22}$$

$$\dot{z}_{r,\text{out}}^P = L_z^{-1} \dot{z}_{r,\text{in}}^P \tag{5.23}$$

$$\dot{z}_{r,\text{out}}^Q = L_z^{-1} \dot{z}_{r,\text{in}}^Q \tag{5.24}$$

Interactive interconnected model Eqs. (5.22)-(5.24), which is formed from a set of linear ODEs, provides several advantages. The model's linearity facilitates system-wide control and scalability, and it dynamically computes the outgoing interaction variables at each time instant. The model does not require the system to reach an equilibrium state for effective operation. Unlike DAE models, this ODE form does not require additional conditions to resolve algebraic singularities, provided that the graph connectivity ensures the existence of L_z^{-1}. The directness of the ODEs also implies a causal relationship between variables as changes in one layer directly affect the outgoing variables, following a predictable cause-and-effect behavior between the neighboring components. This inherent causality simplifies system analysis and control design because each subsystem's response to perturbations is more easily traceable.

Although each subsystem interacts with others bidirectionally, the causal relationships between them are achieved through unidirectional information flow at a given time instant. This predictable cause-and-effect scheme means that changes in one component at time t affect other connected components at time t, simplifying control and analysis. In practice, while information is exchanged bidirectionally between subsystems, the propagation of effects is predictable and traceable, allowing for the identification and isolation of potential

disturbances or faults. This combination of linearity, predictable causality, and the absence of algebraic singularities makes Eqs. (5.22)-(5.24) ODE model robust and efficient tool for multi-layered aggregated system control.

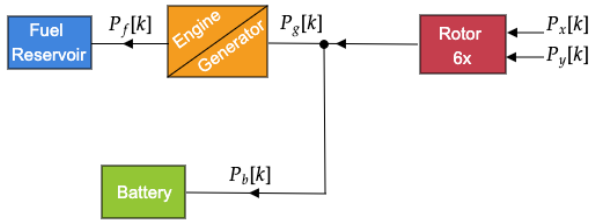

(a) Unidirectional control and information layer exchange

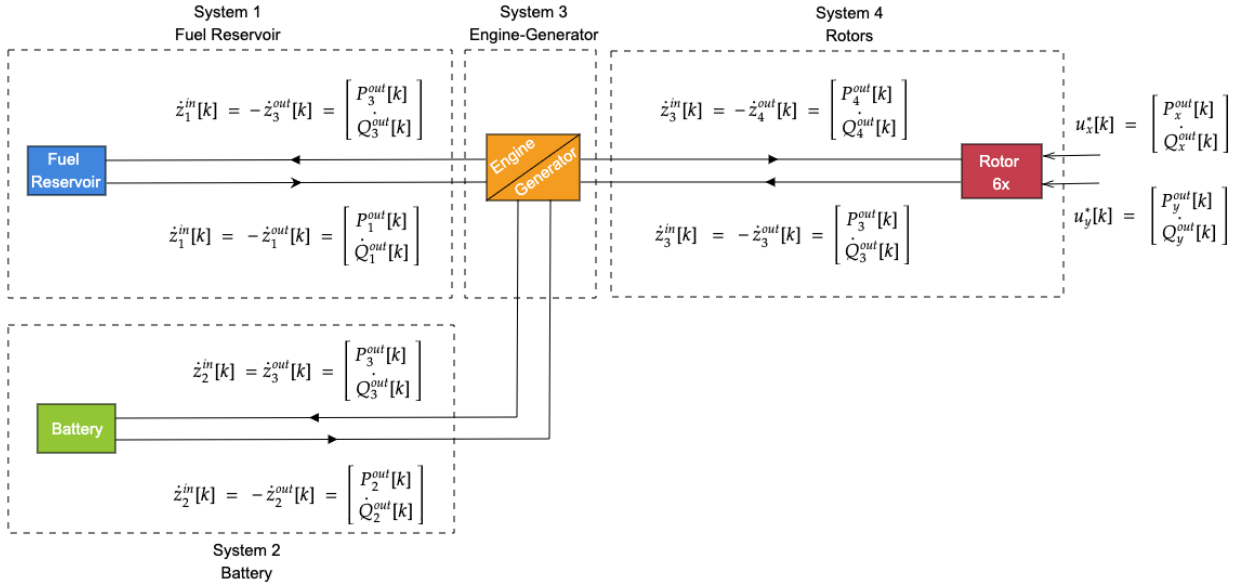

(b) Bidirectional control and information layer interactive exchange

Figure 5.2: Two different paradigms of information exchange

5.4 Distributed Information Exchange Battery Regulation

From the modeling framework of energy state-space immediately follows a distributed information exchange. From there the choice of nature of control is a consequence. The two control approaches introduced, are distributed and decentralized, both designed for the battery following the notation from Fig. 5.2b.

Distributed Battery Control for Powertrain Regulation

Distributed control of the battery within the powertrain regulation framework refers to the power flow management supplemented by the battery using local but also information that is not directly and locally observable information e.g. component A is not directly connected to component B but they can exchange information. Under the assumption that the battery is the interface constrained by the initial state of charge and without internally stored energy conversion the bidirectional information exchange from the Fig. 5.2b becomes the unidirectional real power exchange. Given the problem of maximizing fuel savings and with the energy state-space modeling approach, the optimization problem is formulated to maximize the total power output P_2 and based on notation from the Fig. 5.2b

$$\max_{\beta} \sum_{k=0}^{N} P_2[k]$$

subject to the power output relationship

$$P_2^{out}[k] = P_4^{out}[k] - \beta_k P_3^{out}[k]$$

and the energy constraint over the operation period

$$\sum_{k=0}^{N} P_2[k]\Delta T \leq E_2^{tot}$$

where β_k is the control variable within the bounds:

$$\beta_k \in [0, 1]$$

This can be written more compactly as

$$\max_{\beta} \sum_{k=0}^{N} P_2[k] \tag{5.25}$$

$$s.t.\ P_2^{out}[k] = P_4^{out}[k] - \beta_k P_3^{out}[k] \tag{5.26}$$

$$\sum_{k=0}^{N} P_2[k]\Delta T \leq E_2^{tot} \tag{5.27}$$

$$\beta_k \in [0, 1] \tag{5.28}$$

Here, E_3^{tot} represents the total energy available from the battery, which can be calculated based on the battery's capacity in $[mAh]$, interface voltage, and the period over which the battery is used.

In this control scheme, the battery system actively adjusts the discharge of the current based on the demands of the UAV's flight conditions and power produced from the generator. The regulation is solely based on anticipated power demand and generator output power without the knowledge of what would be the "best" for the generator or the powertrain behavior. This makes the control of the battery to be non-cooperative as it is trying to maximize its participation but without the knowledge of what would be the best for the other components namely the generator and ICE. Direct input on transients from this change of battery behavior on the powertrain's current state, as it is assumed that transients are instantaneous due to the same sampling time of each component (sampling period effectively smooths any transients that could've been captured from the evolution of the powertrain components at different rates of their internal processes).

Decentralized Battery Control for Powertrain Regulation

The decentralized approach leverages local interactions between directly connected components, where the generator, acting as an aggregator, adaptively determines what would be the needed power from the other parts of the system, e.g. supplemental power needed from the battery. This coordination ensures that additional power, under the assumption that the battery is sufficiently charged, is supplied in the required amount and when the generator requires support, enhancing the system's responsiveness to fluctuating demands.

The core of this regulatory control is the dynamical demand power redistribution between the generator and the battery based on a real-time operation where components interactively exchange real power. Unlike distributed control, decentralized interactive aggregated regulation uses local information to determine how each component will interact with other components. This exchange captures both the cause and effect of changing power set points between components, facilitating a more adaptive response to unexpected disturbances or sudden changes in flight conditions.

The optimization is still computed at the battery side, and the generator/engine serves as the aggregator to send set points to the battery depending on the demand. Optimization

is as follows

$$\max_{P_2[k]} \quad \sum_{k=0}^{N} P_2[k] \tag{5.29}$$

$$\text{subject to} \quad P_2[k] \leq P_{\text{sup}}[k] \quad \forall k \tag{5.30}$$

$$P_2[k] \geq P_{2,min}^{out}[k] \quad \forall k \tag{5.31}$$

$$\sum_{k=0}^{N} P_2[k] \cdot \Delta T \leq E_2^{\text{tot}} \tag{5.32}$$

Numerical Results

This chapter presents the numerical results obtained from simulation experiments designed to evaluate the performance of the proposed models and control strategies for hybrid powertrain UAVs. The system is discretized with a timestep ΔT that corresponds to the sampling time of measurements. For simulation purposes, between measurements, the Runge-Kutta 45 (RK45) method was used for more accurate integration of the differential equations. However, for illustrative purposes, the following equations represent a simple Forward-Euler discretization

$$x_{k+1} = x_k + \Delta T \cdot v_{x,k} \tag{6.1}$$

$$y_{k+1} = y_k + \Delta T \cdot v_{y,k} \tag{6.2}$$

$$v_{x,k+1} = v_{x,k} + \Delta T \left(\frac{1}{m} F_{x,k} - \frac{b_x}{m} v_{x,k} \right) \tag{6.3}$$

$$v_{y,k+1} = v_{y,k} + \Delta T \left(\frac{1}{m} F_{y,k} - \frac{b_y}{m} v_{y,k} \right) \tag{6.4}$$

$$f_{k+1} = f_k + \Delta T \left(-\alpha F_{x,k} v_{x,k} - \beta F_{y,k} v_{y,k} - \gamma P_{b,k} - \frac{1}{T_f} f_k \right) \tag{6.5}$$

6.1 Parameter Estimation

This section's results are based on the joint state-parameter estimation EKF method from Chapter 2 on data-informed estimation. The average values of the estimated parameters from Figs. 6.1-6.4 are shown in Tables 6.1-6.2. As the true values of parameters are not known, the validation analysis of estimated parameters is left for future work. The average values of the found parameters Table 6.1-6.2 were used for the composite near-optimal regulation control task.

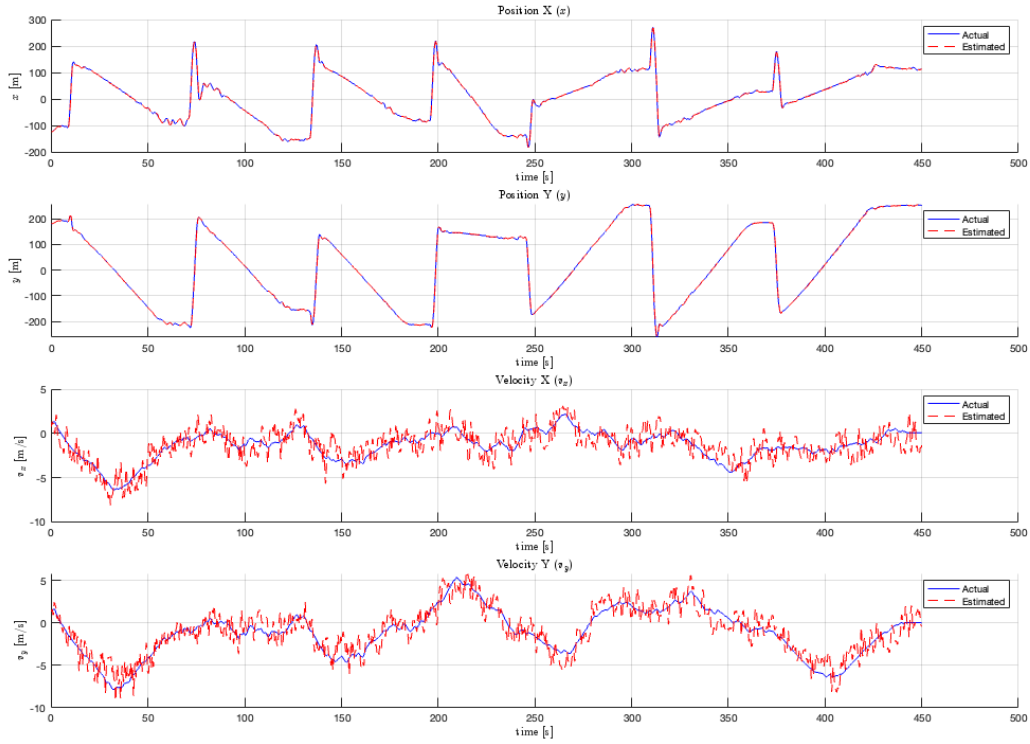

Figure 6.1: Fast subsystem states estimates

Table 6.1: Fast Subsystem Parameters

Fast Subsystem Parameters		
m [kg]	b_x [N·s/m]	b_y [N·s/m]
17.4869	1.9072	0.7021

6.2 Composite Near-Optimal Regulation

In this section, the results of implementing composite near-optimal regulation policies are detailed. The focus is on how these strategies enhance the UAV's performance by optimizing energy usage and improving dynamic response under the knowledge of disturbance. The section shows the results of the use of the disturbance in near-optimal regulation, comparing two LQR approaches with baseline unknown policy used in data collection to highlight improvements in fuel savings.

For the parameters of the system given in Tables (6.1-6.2) a comparison is made, on the fuel level at the end of the flight of two online LQR policies against the unknown policy that was implemented during data collection experiments. The first of the two policies is the

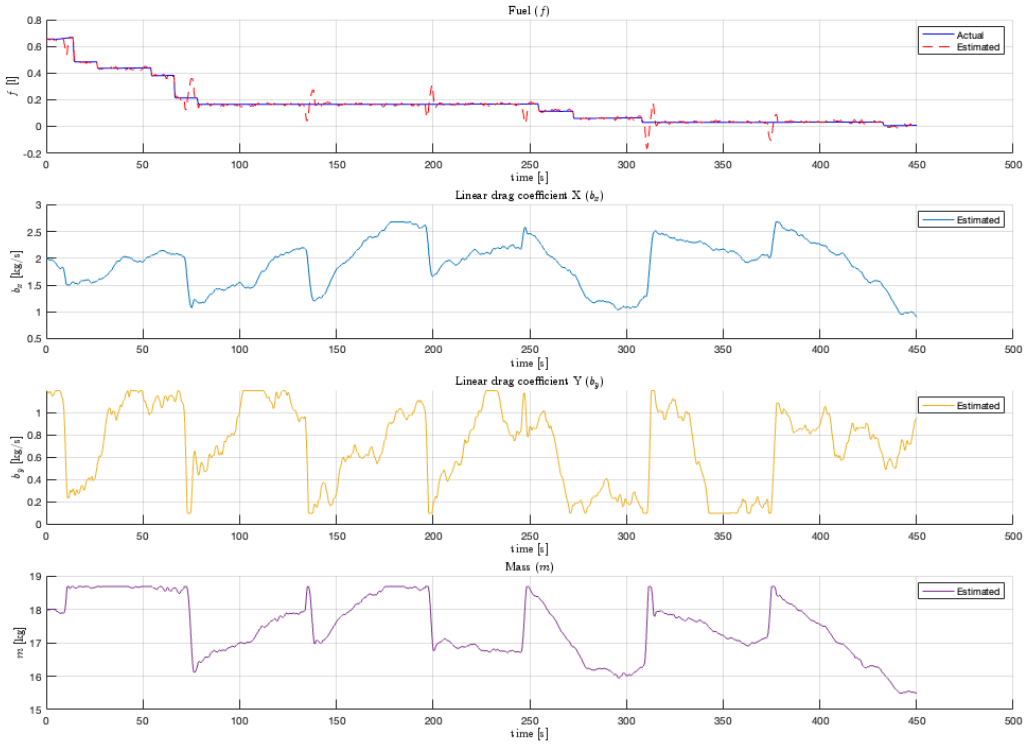

Figure 6.2: Fuel state estimate and fast subsystem estimated parameters

Table 6.2: Slow Subsystem Parameters

Slow Subsystem Parameters			
α [l/sW]	β [l/sW]	γ [l/sW]	T_f [1/s]
7.541e-6	2.289e-6	7.23e-4	398.2434

LQR without disturbance information, which is referred to as the "blind" and the second is the "aware" LQR, as it has information about battery power disturbance on the fuel flow. Time-scale separation is applied and discretization time-step is equal to the sampling rate of $\Delta T = 0.1\ s$. Once the control is computed for each of the subsystems separately, using Eqs. (4.8)-(4.11), separate controls are added and applied to the model of the whole system Eqs. (4.12)-(4.16). As the LQR isn't constrained, the constraints on the system evolution are then based on the system maximum and minimum value of the rate of change of state coming from the provided flight data.

Figure 5.1 shows the lateral drone trajectory in xy-plane during the cruise period of the flight mission with an unknown control input. The trajectory is presented with red dashed arrows that show the direction of the drone's flight, portraying the drone's movement over

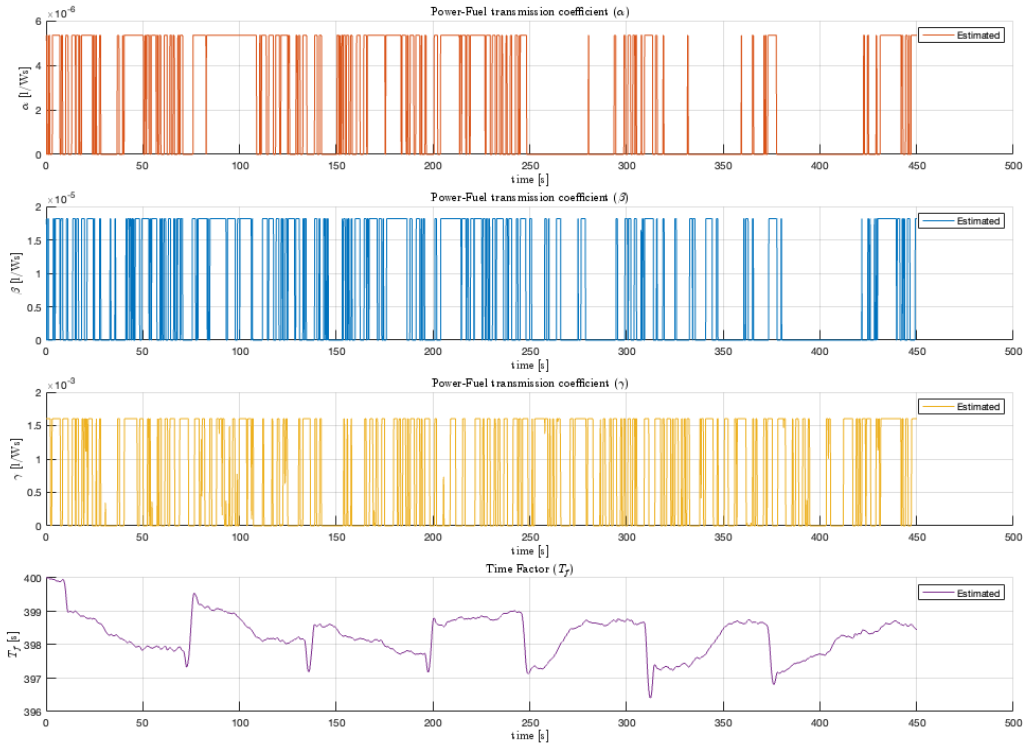

Figure 6.3: Slow subsystem estimated parameters

time. The green dot shows the starting and the blue dot ending point of the flight mission. The trajectory contains loops and changes in direction, which implies complex maneuvers. The path does not appear to be smooth, potentially indicating that the drone experienced disturbances and that the lateral control policy was not optimized. Based on the hypothesis that currently implemented drone control doesn't optimize for fuel savings, figure 6.5 shows how LQR control policies have more leftover fuel at the end of the flight compared to the unknown policy. In Fig. 6.6 one can observe how optimal control saved approximately $3.5 - 4.5\%$ of the fuel level that the drone started the cruise phase of the flight, where range depends on if it is blind or disturbance-aware policy, which as expected shows to be the best fuel-saving policy.

These results show that different energy sources play a distinct role in the functioning of a drone, and that battery effects seen as a disturbance from the standpoint of the fuel reservoir-engine generator can be effectively managed to minimize fuel consumption. The presence of fast and slow control, battery, and fuel engine facilitates the linearization of the model, allowing for separate control computation through time-scale decomposition

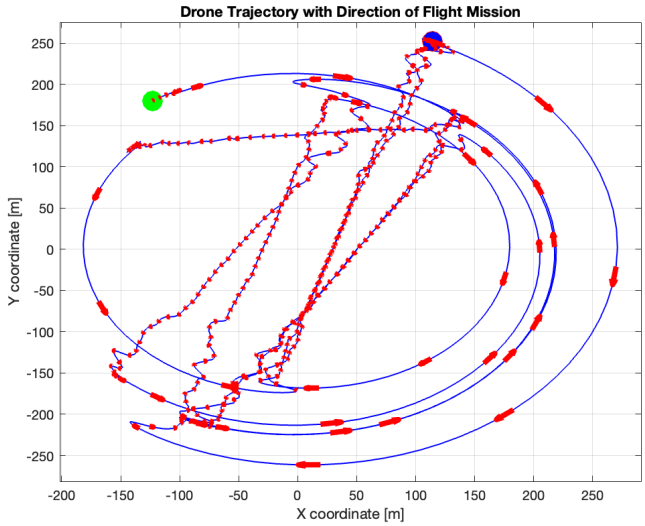

Figure 6.4: Trajectory of the drone in xy-plane under unknown lateral policy control during the cruise phase of the flight mission

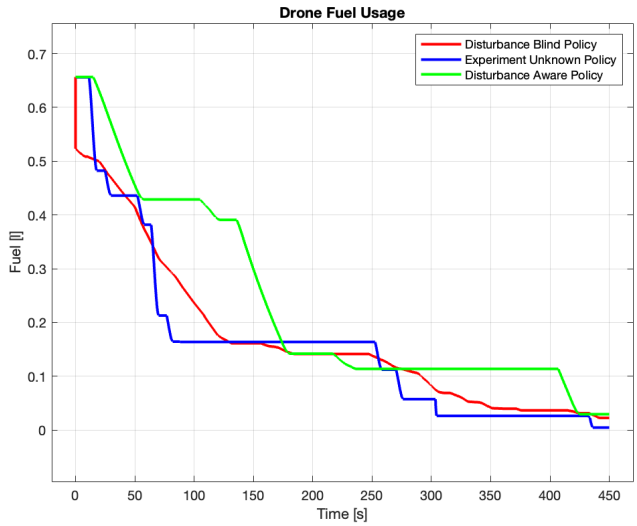

Figure 6.5: Reservoir fuel during the cruise phase of the flight mission

6.3 Distributed Battery Control for Powertrain Regulation

Results of distributed information flow are shown, and how the supplemental powertrain regulation affects then consequently fuel in the reservoir during the flight. Simulations are conducted to test the hypothesis that a distributed control of the powertrain components contributes to fuel savings through cooperative control.

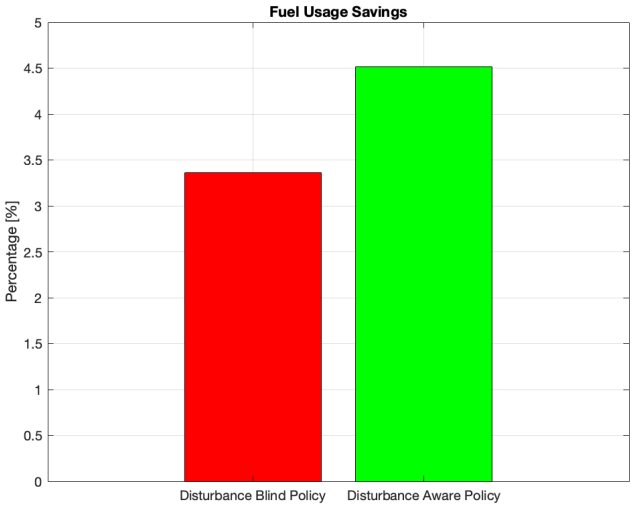

Figure 6.6: Leftover fuel in the reservoir at the end of the cruise phase comparison a) battery blind policy b) battery aware policy

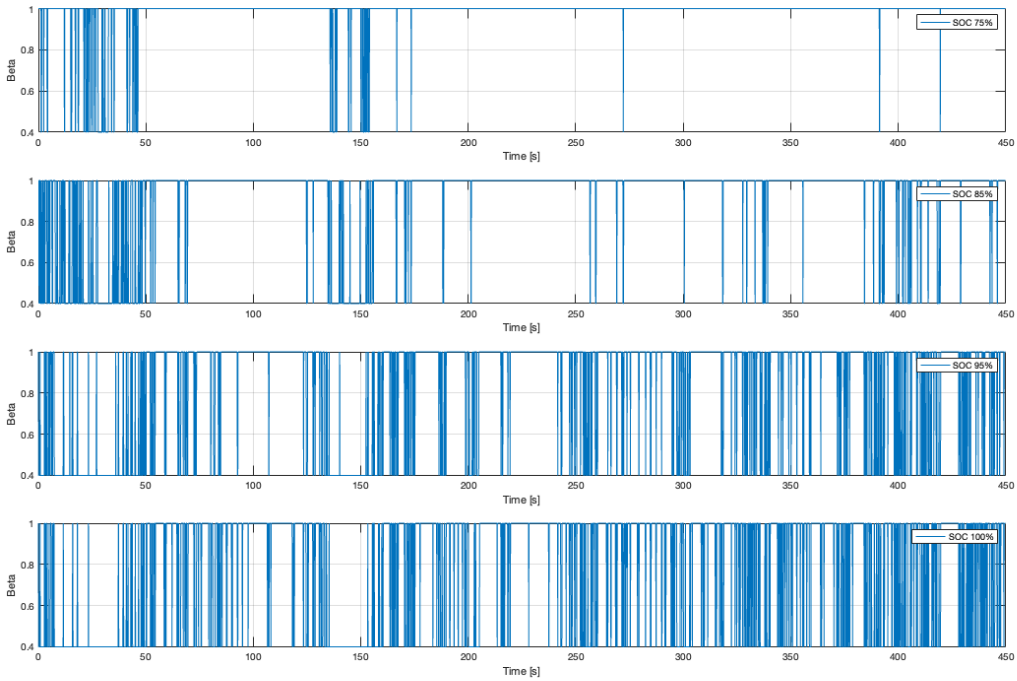

Figure 6.7: Ratio of battery participation β for different initial state-of-charge of battery during the cruise part of the flight with distributed control

Simulation results indicate that the distributed control approach is quite aggressive in reducing the load on the generator. The focus is on increasing the output power of the battery

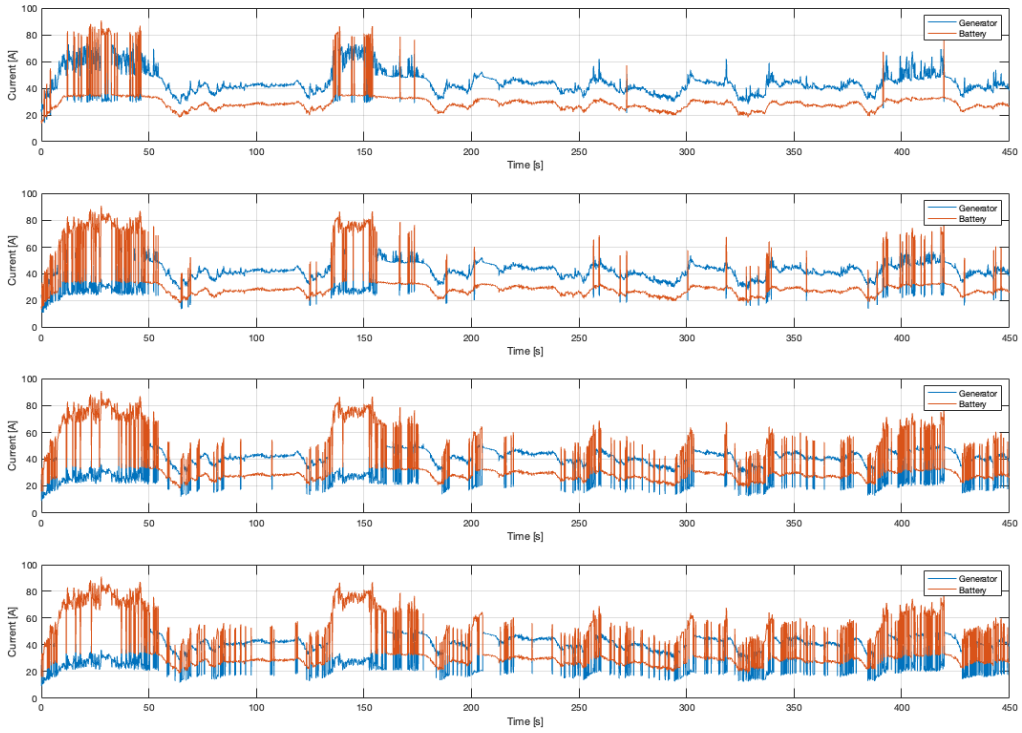

Figure 6.8: Shift of battery and generator current due to distributed control for different initial state-of-charge of battery during the cruise part of the flight

at moments when the load stress is highest on the generator. Thus the power re-distribution during non-standard operation scenarios, with insufficient battery charge, might lead to suboptimal performance of the ICE. With the fully charged battery, distributed control at the end of the cruise phase saves approximately 34.56% of initial fuel in the fuel reservoir.

In summary, distributed control offers simple implementation, but it handles unexpected disturbances or drastic changes in flight conditions quite aggressively compared to decentralized interactive control 6.11.

6.4 Decentralized Battery Control of Powertrain Regulation

Results of decentralized information flow are shown, and how the powertrain regulation affects consequently fuel during the flight. Simulations are conducted to test the hypothesis that decentralized control of the powertrain components contributes to fuel savings through

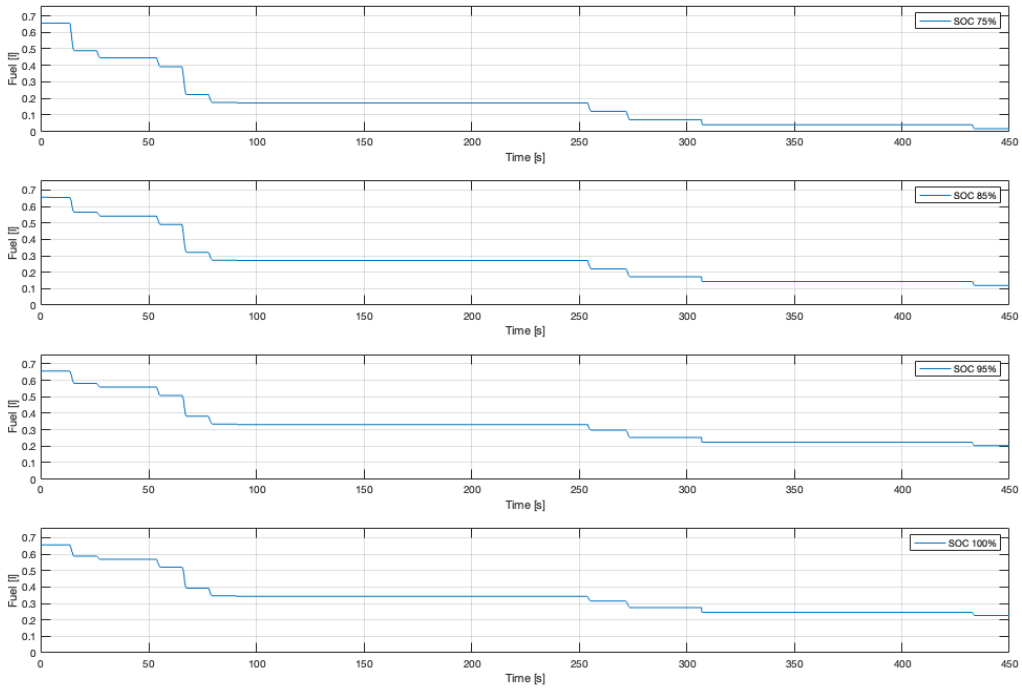

Figure 6.9: Distributed control fuel in the reservoir change during the cruise phase of the flight

cooperative control.

Figure 6.10 was obtained during post-processing and serves as a comparison with 6.7 to show how decentralized control changes the percentage of battery contribution in the total demand.

The simulations show that the decentralized interactive approach not only reduces the load on the generator but also smooths out its generation to ensure optimal generator performance under diverse operational scenarios e.g. unexpected stress as shown in Fig. 2.5. The generator/engine collects flows of nearby modules and computes the supplemental power that the battery should provide to the powertrain. With its primary focus on having a stable and efficient generator and thus ICE operation, to be able to achieve this, control focuses on each horizon time step and proportionally supplements the power. The power that the battery will supplement depends on the initial state of the charge of the battery as can be seen in Fig. 6.11 . By aggregating and analyzing data from various components of the UAV's powertrain, each component adaptively adjusts to changes and thus the system performs better in terms of the fuel usage compared to distributed control. In the situation when the battery is fully charged and assuming that one can fully discharge the battery, as

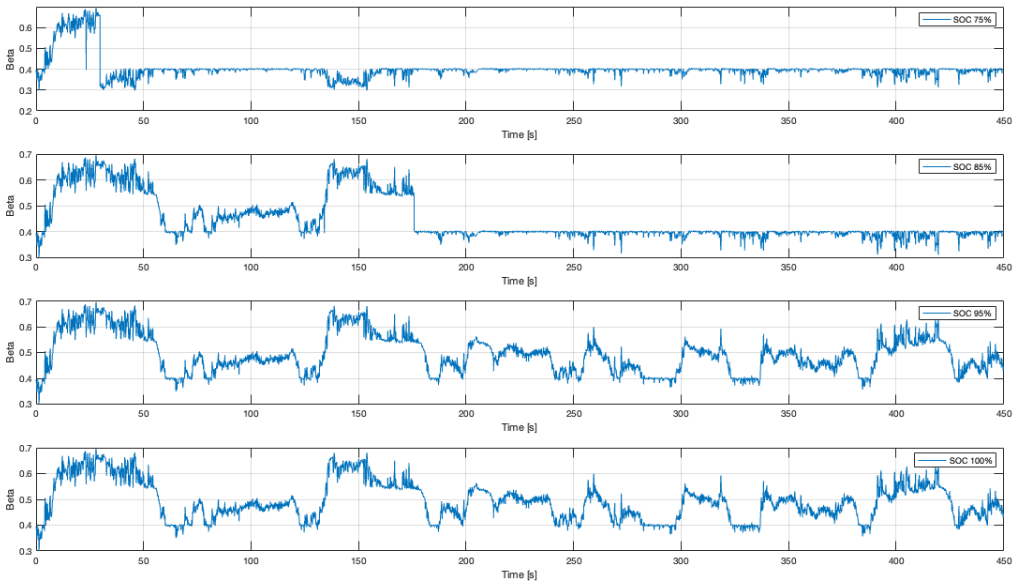

Figure 6.10: Ratio of battery participation β for different initial state-of-charge of battery during the cruise part of the flight

can be seen on the last plot of the Fig. 6.12 at the end of the flight the leftover fuel is around 50.05% the initial volume of the reservoir fuel at the beginning of the cruise phase of the flight.

The primary advantage of this interactive approach lies in its adaptive nature, which allows for each component to decide on interaction with other locally connected components. This makes the system overall more efficient. This enables UAV prolonged autonomy and operational stability under unforeseen environmental factors. However, the complexity of implementing this control can be increased compared to the distributed approach, requiring adaptive algorithms for set point computation.

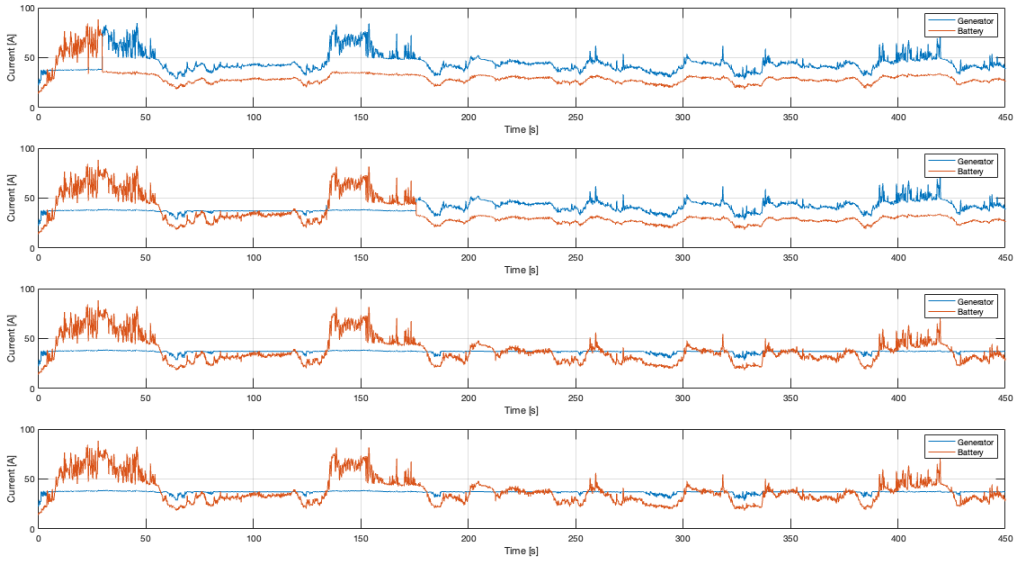

Figure 6.11: Shift of battery and generator current due to decentralized control for different initial state-of-charge of battery during the cruise part of the flight

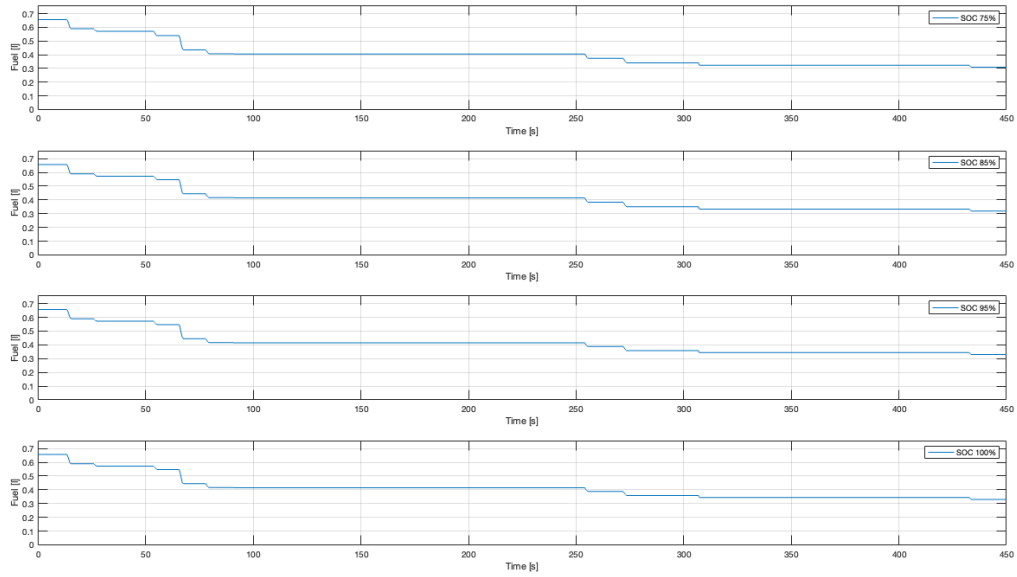

Figure 6.12: Decentralized control fuel in the reservoir change during the cruise phase of the flight

Summary and Future Work

This thesis explored the integration of lateral tracking and powertrain regulation in hexacopter hybrid powertrain UAVs to maximize saved fuel. The work was motivated by observing the data and the question of how optimal ICE operation could be impacted by the passively managed battery. Three different control approaches were compared, and the problem of distributed information flow could outperform centralized information. The main difference is how the control approach looks at each component in isolation or cooperation with other components. Depending on the control context the component might treat other components as the disturbance or as the cooperative component.

The core contributions of this thesis include the development of a novel modeling approach that integrates energy conversion dynamics with the mechanical dynamics of the drone, estimated using flight-mission data. Additionally, the thesis has shown a data-informed approach for nonlinear dynamics parameter estimation, which confirmed timescale separation. Using the average-model parameters, a composite Linear Quadratic Regulator (LQR) with predictive control was implemented, achieving 4.5% of fuel savings by recognizing and adjusting control policy to battery disturbances in a centralized setup.

Further analysis compared this centralized approach with two slightly different approaches, first distributed and second decentralized information flow within the UAV powertrain. The distributed approach facilitated supplement power from the battery, reducing the demand on the generator and consequently ICE, but this control due to lack of coordination is shown to be aggressive and overly trying to compensate the generator part of the load thus becoming non-cooperative for the interconnected system. On the other hand, the decentralized approach involved interactive, aggregated powertrain regulation where the aggregator (generator/engine in Fig. 5.2b) determined the supplemental power needed from the battery, adapting to demand changes and reducing fuel usage through increased battery power output. This approach's effectiveness is in each component adaptive adjustment and coordination based on the local information exchange that depends on the direct local connections. This enables components to decide for themselves how much real power they want and need to exchange, thus facilitating true cooperation.

In the simulation, the distributed control saved 34.56% of the initial amount of fuel in the reservoir during the cruise phase with a fully charged battery, while the decentralized control outperformed all other methods, reaching up to 50.05% fuel savings. Overall, this thesis demonstrated that decentralized and distributed control approaches could significantly enhance the operational efficiency of hybrid powertrain UAVs, providing robust solutions to improve fuel economy and reduce the impact of disturbances on ICE performance.

In future work, the focus will be on the following two topics, which are currently work in progress.

Trajectory Optimization in Energy-State Space

The current project is at the moment being extended to include a model for energy-efficient trajectory optimization with a focus on formulating the UAV optimization problem in an energy-state space framework. Also, in future work, the focus will shift towards exploring the potential of energy state space in modeling disturbances outside of the powertrain. Combined extended disturbance modeling is expected to provide the spatial understanding of energy-efficient paths and accordingly optimize the drone movement based on mission requirements under environment disturbances e.g. wind disturbance subject to linear energy system dynamics.

Fail-Safe Communication Mechanisms

The question of fail-safe communication mechanisms in energy state space during critical situations is an important aspect of the research which will delve into the mechanisms of local communication, and fail-safe mechanisms within the energy state space, particularly how different components of a decentralized system interact and contribute to the overall energy efficiency in critical situations for the system. The work will explore strategies that enable these components to independently respond to local disturbances while aligning with the global control objectives, thereby enhancing the robustness and adaptability of the UAV system.

References

[1] T. Lei, Z. Yang, Z. Lin, and X. Zhang, "State of art on energy management strategy for hybrid-powered unmanned aerial vehicle," *Chinese Journal of Aeronautics*, 2019. [Online]. Available: https://api.semanticscholar.org/CorpusID:128024162.

[2] H. Zhang, C. Saudemont, B. Robyns, and M. Petit, "Comparison of technical features between a more electric aircraft and a hybrid electric vehicle," in *2008 IEEE Vehicle Power and Propulsion Conference*, 2008, pp. 1–6. DOI: 10.1109/VPPC.2008.4677663.

[3] C. Di Franco and G. Buttazzo, "Energy-aware coverage path planning of uavs," in *2015 IEEE international conference on autonomous robot systems and competitions*, IEEE, 2015, pp. 111–117.

[4] F. Morbidi, R. Cano, and D. Lara, "Minimum-energy path generation for a quadrotor uav," in *2016 IEEE International Conference on Robotics and Automation (ICRA)*, IEEE, 2016, pp. 1492–1498.

[5] A. Abdilla, A. Richards, and S. Burrow, "Power and endurance modelling of battery-powered rotorcraft," in *2015 IEEE/RSJ international conference on intelligent robots and systems (IROS)*, IEEE, 2015, pp. 675–680.

[6] M. Yazid, H. Bouadi, N. Hamdadou, and N. Hebablia, "Hexarotor attitude stabilization based feedback linearization and sliding mode controllers," in *2021 29th Mediterranean Conference on Control and Automation (MED)*, 2021, pp. 1143–1148. DOI: 10.1109/MED51440.2021.9480206.

[7] M. Podhradskỳ, C. Coopmans, and A. Jensen, "Battery state-of-charge based altitude controller for small, low cost multirotor unmanned aerial vehicles," *Journal of Intelligent & Robotic Systems*, vol. 74, pp. 193–207, 2014.

[8] K. Dorling, J. Heinrichs, G. G. Messier, and S. Magierowski, "Vehicle routing problems for drone delivery," *IEEE Transactions on Systems, Man, and Cybernetics: Systems*, vol. 47, no. 1, pp. 70–85, 2017. DOI: 10.1109/TSMC.2016.2582745.

[9] S. Poikonen, X. Wang, and B. Golden, "The vehicle routing problem with drones: Extended models and connections," *Networks*, vol. 70, no. 1, pp. 34–43, 2017.

[10] Y. Chen, D. Baek, A. Bocca, A. Macii, E. Macii, and M. Poncino, "A case for a battery-aware model of drone energy consumption," in *2018 IEEE International Telecommunications Energy Conference (INTELEC)*, 2018, pp. 1–8. DOI: 10.1109/INTLEC.2018.8612333.

[11] M. N. Boukoberine, T. Donateo, and M. Benbouzid, "Optimized energy management strategy for hybrid fuel cell powered drones in persistent missions using real flight test data," *IEEE Transactions on Energy Conversion*, vol. 37, no. 3, pp. 2080–2091, 2022. DOI: 10.1109/TEC.2022.3152351.

[12] D. Aleksandrov and I. Penkov, "Energy consumption of mini uav helicopters with different number of rotors."

[13] G. Hattenberger, M. Bronz, and J.-P. Condomines, "Evaluation of drag coefficient for a quadrotor model," *International Journal of Micro Air Vehicles*, vol. 15, p. 17 568 293 221 148 378, 2023.

[14] R. Jaddivada, "A unified modeling for control of reactive power dynamics in electrical energy systems," Ph.D. dissertation, Massachusetts Institute of Technology, 2020.

[15] H. M. Paynter, "Analysis and design of engineering systems," *MIT press*, 1961.

[16] J. J. Ruiz, M. Pulido, and T. Miyoshi, "Estimating model parameters with ensemble-based data assimilation: A review," *Journal of the Meteorological Society of Japan. Ser. II*, vol. 91, no. 2, pp. 79–99, 2013.

[17] L. Ljung, "Asymptotic behavior of the extended kalman filter as a parameter estimator for linear systems," *IEEE Transactions on Automatic Control*, vol. 24, no. 1, pp. 36–50, 1979.

[18] University of Toronto, *Compactness and applications*, https://www.math.toronto.edu/courses/mat237y1/20189/notes/Chapter1/S1.4.html#sect-1.4.2, 2018.

[19] E. Abed, "Decomposition and stability for multiparameter singular perturbation problems," *IEEE transactions on Automatic Control*, vol. 31, no. 10, pp. 925–934, 1986.

[20] J. Chow and P. Kokotovic, "A decomposition of near-optimum regulators for systems with slow and fast modes," *IEEE Transactions on Automatic Control*, vol. 21, no. 5, pp. 701–705, 1976. DOI: 10.1109/TAC.1976.1101342.

[21] J. Chow and P. Kokotovic, "Two-time-scale feedback design of a class of nonlinear systems," *IEEE Transactions on Automatic Control*, vol. 23, no. 3, pp. 438–443, 1978. DOI: 10.1109/TAC.1978.1101736.

[22] S. Pfrommer and S. Sojoudi, "Lqr control with sparse adversarial disturbances," in *2022 IEEE 61st Conference on Decision and Control (CDC)*, IEEE, 2022, pp. 2346–2353.

[23] D. Bertsekas, *Dynamic programming and optimal control: Volume I*. Athena scientific, 2012, vol. 4.

[24] G. Goel and B. Hassibi, "The power of linear controllers in lqr control," in *2022 IEEE 61st Conference on Decision and Control (CDC)*, IEEE, 2022, pp. 6652–6657.

[25] M. D. Ilić, L. Xie, U. A. Khan, and J. M. Moura, "Modeling of future cyber–physical energy systems for distributed sensing and control," *IEEE Transactions on Systems, Man, and Cybernetics-Part A: Systems and Humans*, vol. 40, no. 4, pp. 825–838, 2010.

[26] J. C. Willems, "The behavioral approach to open and interconnected systems," *IEEE control systems magazine*, vol. 27, no. 6, pp. 46–99, 2007.

[27] H. A. Gada and M. D. Ilic, *Slow inter-area electro-mechanical oscillations revisited: Structural property of complex multi-area electric power systems*, 2024. arXiv: 2405.08228 [eess.SY].

[28] X. Liu, M. Ilic, M. Athans, C. Vila, and B. Heilbronn, "A new concept of an aggregate model for tertiary control coordination of regional voltages," in *[1992] Proceedings of the 31st IEEE Conference on Decision and Control*, IEEE, 1992, pp. 2934–2940.

[29] R. Lawson and M. Ilic, "Dissipativity conditions for maximum dynamic loadability," *arXiv preprint arXiv:2405.05036*, 2024.

[30] M. D. Ilic, "Interaction variables-based modeling and control of energy dynamics," in *Women in Power: Research and Development Advances in Electric Power Systems*, Springer, 2012, pp. 307–350.